



# Scattering and absorbing aerosols in the climate system

Jing Li<sup>1</sup>✉, Barbara E. Carlson<sup>2</sup>, Yuk L. Yung<sup>3</sup>, Daren Lv<sup>4</sup>, James Hansen<sup>5</sup>, Joyce E. Penner<sup>6</sup>, Hong Liao<sup>7</sup>, V. Ramaswamy<sup>8</sup>, Ralph A. Kahn<sup>9</sup>, Peng Zhang<sup>10</sup>, Oleg Dubovik<sup>11</sup>, Aijun Ding<sup>12</sup>, Andrew A. Lacis<sup>2</sup>, Lu Zhang<sup>1</sup> and Yueming Dong<sup>1</sup>

**Abstract** | Tropospheric anthropogenic aerosols contribute the second-largest forcing to climate change, but with high uncertainty owing to their spatio-temporal variability and complicated optical properties. In this Review, we synthesize understanding of aerosol observations and their radiative and climate effects. Aerosols offset about one-third of the warming effect by anthropogenic greenhouse gases. Yet, in regions and seasons where the absorbing aerosol fraction is high — such as South America and East and South Asia — substantial atmospheric warming can occur. The internal mixing and the vertical distribution of aerosols, which alters both the direct effect and aerosol–cloud interactions, might further enhance this warming. Despite extensive research in aerosol–cloud interactions, there is still at least a 50% spread in total aerosol forcing estimates. This ongoing uncertainty is linked, in part, to the poor measurement of anthropogenic and natural aerosol absorption, as well as the little-understood effects of aerosols on clouds. Next-generation, space-borne, multi-angle polarization and active remote sensing, combined with in situ observations, offer opportunities to better constrain aerosol scattering, absorption and size distribution, thus, improving models to refine estimates of aerosol forcing and climate effects.

Aerosols are small liquid or solid particles suspended in the atmosphere<sup>1</sup>. They can be emitted directly (such as dust, sea salt, black carbon (BC) and volcanic aerosols) or formed indirectly through chemical reactions (including sulfate, nitrate, ammonium and secondary organic aerosols). Owing to their relatively short lifetime, aerosol concentrations typically peak near their sources. Desert regions (such as North Africa and the Middle East), industrial regions (such as East and South Asia) and biomass-burning regions (such as South America and South Africa) are, therefore, characterized by high mass concentrations (FIG. 1). Aerosols exhibit complicated compositions and vary substantially in shape and size, typically ranging between 0.01 and 10  $\mu\text{m}$  (REF.<sup>2</sup>). Depending on these structural and compositional characteristics, aerosols can scatter and/or absorb shortwave radiation, as quantified through the single-scattering albedo (SSA; TABLE 1). Purely scattering aerosols include sulfates, nitrates, ammonium and sea-salt particles, whereas absorbing aerosols are primarily BC, with dust and organic carbon partly absorbing in the ultraviolet (UV) spectrum<sup>3</sup>.

Aerosols have a direct bearing on Earth's energy balance and, therefore, on climate. For instance, aerosol scattering and absorption alters the radiation balance and atmospheric stability through perturbations to the

vertical temperature profile. Aerosols can further serve as cloud condensation nuclei (CCN) or ice-nucleating particles (INPs), which modify the reflectivity and lifetime of clouds through microphysical processes. Collectively, these influences are quantified as aerosol forcing: the change of net radiative flux at a specified level of the atmosphere, often assessed relative to estimated pre-industrial conditions<sup>4</sup>.

Globally, anthropogenic aerosols are estimated to produce a net cooling  $\sim -1.3 \pm 0.7 \text{ W m}^{-2}$  at the top of the atmosphere;  $-0.3 \pm 0.3 \text{ W m}^{-2}$  is attributed to the aerosol–radiation interaction (ARI),  $-1.0 \pm 0.7 \text{ W m}^{-2}$  to aerosol–cloud interactions,  $\sim -1.15 \text{ W m}^{-2}$  to total forcing from scattering aerosols and  $\sim +0.12 \text{ W m}^{-2}$  to BC<sup>4</sup>. This combined aerosol forcing offsets roughly one-third of the warming from anthropogenic greenhouse gases (GHGs). However, the large spread in the estimated aerosol forcing leads to large discrepancies in climate sensitivity<sup>5,6</sup>. Thus, aerosols are considered to be the largest contributor of uncertainty in quantifying present-day climate change<sup>4</sup>.

Much of this uncertainty in aerosol forcing arises from both the lack of separate global constraints on aerosol optical and microphysical properties (optical depth, size distribution, hygroscopicity and mixing state, among others) and the inaccurate representation of them in climate models<sup>7–10</sup>. In particular, aerosol SSA is further

✉e-mail: jing-li@pku.edu.cn

<https://doi.org/10.1038/s43017-022-00296-7>

## Key points

- Climate models indicate at least a 30% uncertainty in aerosol direct forcing and 100% uncertainty in indirect forcing due to aerosol–cloud interactions.
- The amount of aerosol light scattering and absorption, expressed as the aerosol single-scattering albedo parameter, is critical in affecting both aerosol radiation interaction and aerosol–cloud interactions.
- Current satellite sensors cannot provide global-scale 3D single-scattering albedo measurements. Future observational efforts should combine satellite-based, multi-angle polarization sensors and high-spectral-resolution lidars with international aircraft and surface in situ observation networks.
- Direct comparison of radiation properties observed by satellites with those derived from climate models that assimilate aerosol parameters will improve the understanding of aerosol microphysical properties.
- Future work should investigate the mechanisms underlying aerosol–cloud interactions, especially the adjustment of cloud fraction and water for warm clouds and the microphysical processes in ice and mixed-phase clouds.

thought to contribute substantially to the uncertainties in direct aerosol forcing<sup>11,12</sup>, and might even change in sign<sup>13–15</sup>. Despite its importance, aerosol SSA is largely unmeasured by current satellite sensors. However, emerging techniques using high-accuracy, multi-angle polarimetry measurements combined with space-based lidars, and constrained by ground-based remote sensing and detailed in situ measurements of particle microphysical properties, represent a promising way to establish a consistent 3D global SSA record<sup>16–21</sup>. When combined with models, this progress will, thus, improve the modelled aerosol parameters and better quantify aerosol forcing estimates and even climate projections. Moreover, a consistent aerosol observational record will allow improved quantification of the broader environmental impacts of aerosols, including on air pollution and haze, and, in turn, visibility and human health.

In this Review, we focus on the aerosol impacts on climate and synthesize the latest progress in measuring aerosol properties, understanding their spatio-temporal variability and efforts taken to quantify their radiative and climate effects. We describe the challenges remaining in understanding the physical properties and space–time

variability of different aerosol types and propose possible approaches to better constrain aerosol forcing.

## Physical processes impacting climate

Determining the ultimate impact of aerosol forcing on climate is complicated, as aerosols impact the energy balance and the climate system through various pathways. These pathways include direct scattering and absorption of radiation (direct effects) and interaction between these two effects, as well as with clouds, as will now be discussed (FIG. 2).

**Aerosol scattering effect.** The primary effect of aerosols in the climate system is the scattering of solar radiation<sup>1</sup>, which means that only the direction of the radiation changes. Sulfate, nitrate and sea-salt aerosols can be considered purely scattering at visible wavelengths<sup>22</sup>. Most aerosol types are relatively small, generally comparable with or smaller than the wavelength of visible light. As a result, their scattering effect is strongest in the short-wave spectrum and negligible at wavelengths longer than about a micron, with the exception of some large dust particles<sup>23</sup>. This spectral characteristic is distinct from many GHGs, which primarily absorb in the thermal infrared. The scattering increases the fraction of solar radiation reflected back to space, cooling the climate system. However, high surface albedo and the presence of clouds tend to reduce the net effect<sup>12,14,24</sup>. The vertical distribution of aerosols does not change their scattering effect; however, it can impact the radiation balance, for example, by changing the optical path over which water vapour absorption occurs<sup>25</sup> or the aerosol layer vertical location relative to clouds.

The scattering of aerosols also exhibits directional and polarization characteristics. In climate modelling, aerosols are usually assumed to be homogeneous spheres. Light interactions with spherical aerosols are governed by the Mie scattering solution; the degree of forward scattering is often represented by the asymmetry parameter,  $g$  (TABLE 1). Typical  $g$  values for aerosols are between 0.6 and 0.8, indicating primarily forward scattering<sup>26</sup>. Non-spherical particles are generally less efficient at backscattering, resulting in an increased  $g$  value, although the exact phase function can be much more complicated, depending on the particle size, morphology, orientation, surface roughness and so on<sup>27,28</sup>. In addition, radiation scattered by aerosols also exhibits polarization features, and the degree of polarization, as well as the phase function of the polarized component, are sensitive to aerosol type, especially aerosol shape, and absorption<sup>29</sup>. The linear depolarization ratio (TABLE 1) is zero for homogeneous spheres but can be much larger for non-spherical particles<sup>28</sup>, which has been used by polarized lidars to distinguish non-spherical dust from spherical particle types<sup>30</sup>. The sky polarization pattern of scattered radiation by absorbing aerosols is mostly different from that of purely scattering aerosols and can be used to retrieve SSA in remote-sensing applications<sup>29,31</sup>.

**Aerosol absorption effect.** Some aerosols also absorb radiation. BC in aerosols makes the largest contribution to aerosol absorption<sup>32</sup>, with nearly flat spectral

## Author addresses

<sup>1</sup>Laboratory for Climate and Ocean–Atmosphere Studies, Department of Atmospheric and Oceanic Sciences, School of Physics, Peking University, Beijing, China.

<sup>2</sup>NASA Goddard Institute for Space Studies, New York City, NY, USA.

<sup>3</sup>Division of Geological and Planetary Sciences, California Institute of Technology, Pasadena, CA, USA.

<sup>4</sup>Laboratory for Middle Atmosphere and Global Environment Observation (LAGEO), Institute of Atmospheric Physics, Chinese Academy of Sciences, Beijing, China.

<sup>5</sup>The Earth Institute, Columbia University, New York, NY, USA.

<sup>6</sup>Department of Climate and Space Sciences and Engineering, University of Michigan, Ann Arbor, MI, USA.

<sup>7</sup>Jiangsu Key Laboratory of Atmospheric Environment Monitoring and Pollution Control, Collaborative Innovation Center of Atmospheric Environment and Equipment Technology, School of Environmental Science and Engineering, Nanjing University of Information Science and Technology, Nanjing, China.

<sup>8</sup>NOAA Geophysical Fluid Dynamics Laboratory, Princeton, NJ, USA.

<sup>9</sup>Earth Sciences Division, NASA Goddard Space Flight Center, Greenbelt, MD, USA.

<sup>10</sup>National Satellite Meteorological Center, Innovation Center for Fengyun Meteorological Satellite, China Meteorological Administration (CMA), Beijing, China.

<sup>11</sup>Laboratoire d'Optique Atmosphérique, Université de Lille, CNRS, Lille, France.

<sup>12</sup>School of Atmospheric Sciences, Nanjing University, Nanjing, China.

behaviour at visible wavelengths<sup>33</sup>. Dust and organic carbon aerosols strongly absorb in the UV range, but this absorption quickly becomes negligible beyond ~600 nm (REFS<sup>33,34</sup>). Aerosol absorption leads to a positive radiation balance anomaly in the climate system and contributes to atmospheric warming. At the surface, however, the effect is generally still cooling, as the aerosol heating occurs higher in the atmosphere<sup>35</sup>. The atmospheric heating tends to increase atmospheric stability, degrade air quality and slow the hydrological cycle<sup>15,36–38</sup>, which might induce a positive feedback of aerosol climate effects by decreasing aerosol wet deposition.

The effect of aerosol absorption also depends on the surface albedo and the presence of clouds, and can, therefore, be more complicated. In general, absorbing aerosols appear relatively darker over brighter surfaces, which tends to enhance the net effect of atmospheric absorption<sup>12</sup>. Under a cloudy sky, when the aerosols are located above clouds, the atmospheric absorption is greatly enhanced, similar to the case of aerosols above a bright underlying surface. In contrast, aerosol-induced absorption will be weakened if the cloud is above the absorbing aerosol layer and even approaches zero as the cloud becomes thicker<sup>39</sup>, as much of the incoming radiation will be reflected or attenuated by the cloud before reaching the aerosols<sup>40,41</sup>.

The vertical distribution of absorbing aerosols is also critical in determining their radiative effect<sup>42</sup>, and this factor is coupled with the surface albedo effect. Under clear sky, with a lightly reflecting surface, if absorbing aerosols are located at a higher altitude, more incoming radiation is available there than at low altitudes for absorption<sup>43</sup>, which induces a stronger warming effect. However, if the surface is sufficiently bright, such as over snow, the interaction of absorbing aerosols with surface-reflected radiation can become the dominant term, and, thus, a lower absorbing aerosol layer height might induce a stronger warming effect<sup>25</sup>.

Absorbing aerosols themselves can change the underlying surface albedo by depositing on bright surfaces such as snow and ice<sup>44,45</sup>. This albedo reduction results in a warming of the surface and contributes to processes such as Arctic ice melting<sup>46</sup> and Himalayan glacier retreat<sup>47</sup>.

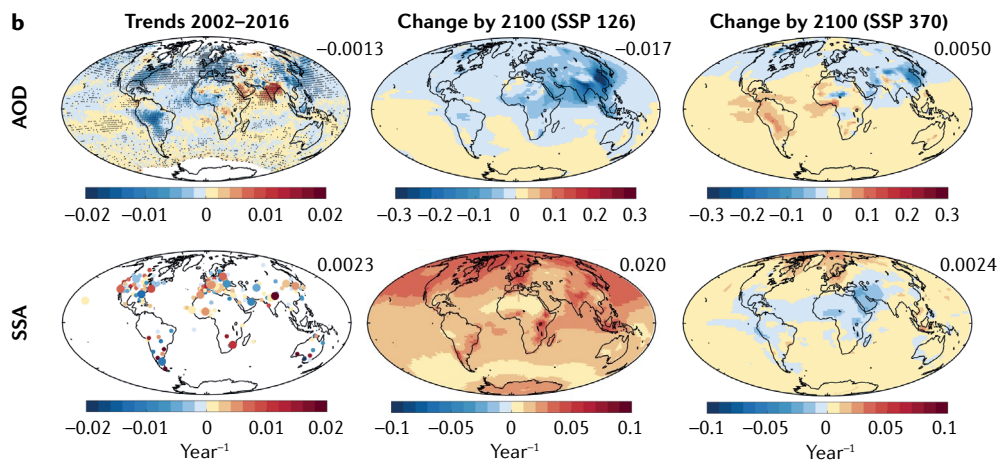
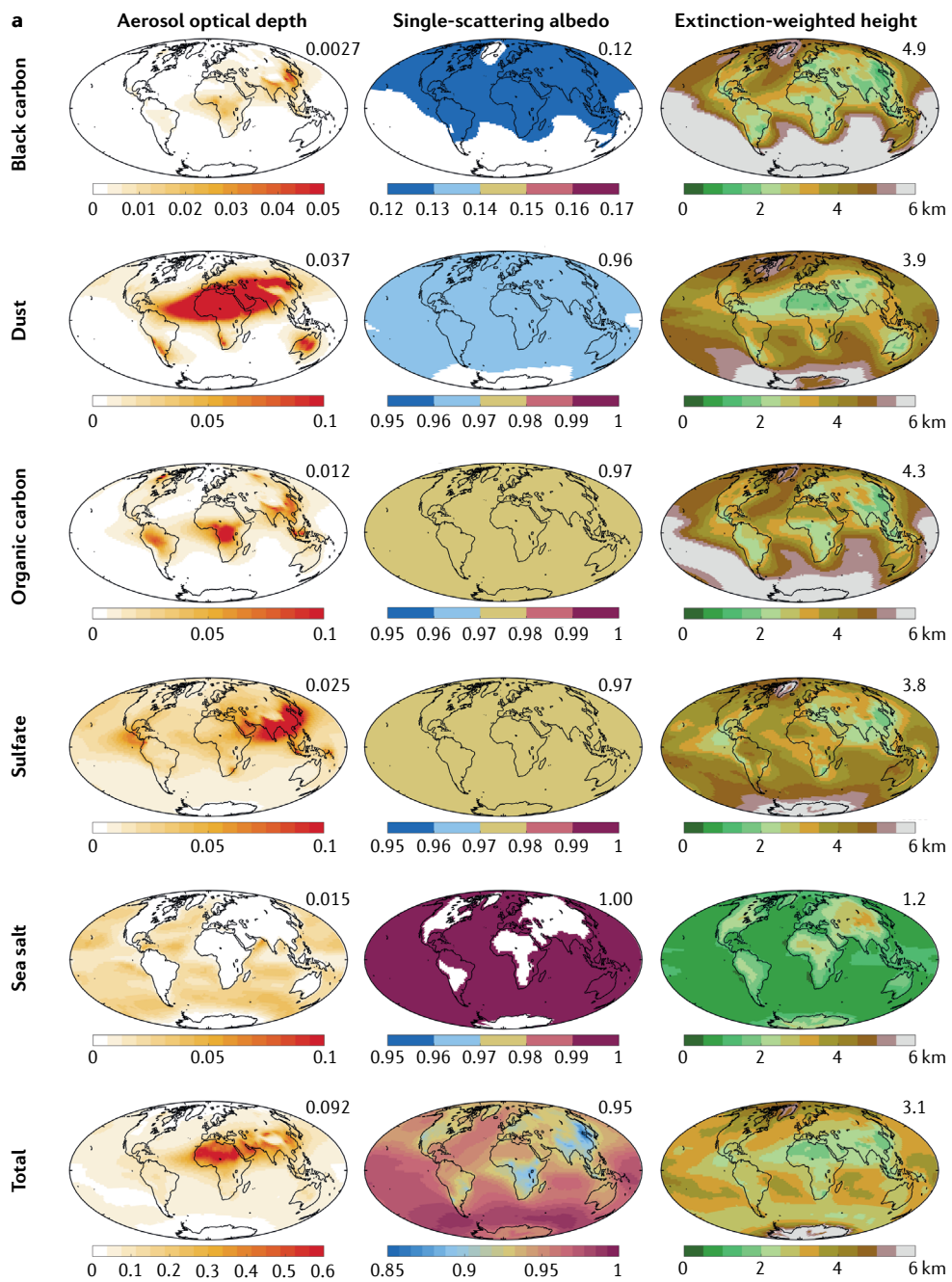
**Combined effect of scattering and absorbing aerosols and their interaction.** Purely scattering and light-absorbing aerosols frequently coexist and, because many of their radiative effects are opposite, their combined effect is complicated and uncertain. The ratio of aerosol scattering to absorption, characterized by the SSA, thus critically determines the magnitude and the sign of the aerosol forcing<sup>48</sup>. Typical SSA values found at worldwide locations are between 0.8 and 1 (REF.<sup>26</sup>), with lower values indicating a tendency towards a warming effect. The critical SSA, below which the overall aerosol effect will shift from negative to positive, is generally between 0.85 and 0.95 at 550 nm (REFS<sup>13,49</sup>), and is typically higher over brighter surfaces or under cloudy sky conditions<sup>15,50</sup>.

Absorbing and purely scattering aerosols interacting with each other produce additional complications. One scenario is the internal or core-shell mixing of BC

with scattering aerosols that are often found in fossil fuel and biomass-burning emissions; this internal mixing enhances BC absorption by 1–2.5 times, depending on the structure and morphology of the mixture<sup>51–54</sup>. Another scenario is through the vertical distribution; when scattering aerosols are concentrated below absorbing aerosols, the net aerosol absorption can be strengthened, and vice versa, analogous to the absorbing aerosol-over-cloud case. This vertical superposition of aerosol layers results in a combined direct forcing that might be different from the sum of the direct forcing of individual aerosol components. This nonlinear effect accounts for 14% of the total clear sky aerosol direct forcing globally, but can reach 100% regionally<sup>55</sup>.

**Aerosol–cloud interaction.** Aerosols can serve as CCN and change cloud microphysical properties. Water-soluble aerosols, such as sulfate, nitrate, sea salt and secondary organic aerosols, are more efficient CCN than insoluble species (mainly dust and organic aerosols having high BC content), making them major players in aerosol–cloud interaction<sup>56</sup>. The aerosol impact on warm clouds is complicated and involves several processes. The immediate effect of an increase in aerosol number concentration is to increase the number of cloud droplets and, thus, cloud reflectivity, known as the Twomey effect<sup>57</sup>. The Twomey effect typically cools the climate, as more cloud droplets tend to reflect more radiation back to space. Subsequently, cloud fraction and liquid water path (LWP) adjust in response to the increase of cloud droplets, which further impact the radiative effects of aerosol-perturbed clouds<sup>9</sup>. On the one hand, aerosol perturbation tends to produce more cloud droplets with smaller size that take longer to precipitate, thereby, increasing LWP and resulting in a cooling effect. On the other hand, these smaller droplets are easier to evaporate, which also enhances the mixing of clouds with ambient dry air. This effect reduces LWP and, thus, causes a warming effect<sup>9</sup>. Other factors, such as meteorological conditions, also complicate the LWP adjustment<sup>58</sup>. As a result, various relationships between cloud droplet number and LWP have been observed<sup>59–62</sup>. Globally, it is likely that the above two competing effects offset each other, so the overall effect of LWP adjustment in response to increased aerosols is weak<sup>63</sup>.

Aerosols can also act as INPs and impact both ice and mixed-phase clouds, especially for the intermediate absorbing species of dust and organic aerosols<sup>64,65</sup>. BC is more absorptive and could also act as an INP, but this potential function is controversial and might be negligible relative to background INPs<sup>66</sup>. The aerosol–ice–cloud interaction processes are more complicated and less well understood than warm-cloud interactions, especially considering the competing effects of homogeneous freezing from liquid-phase particles and heterogeneous freezing by INPs. If INPs are added to an ice cloud already dominated by heterogeneous freezing, they will lead to more ice crystals and possibly a warming effect. Alternatively, if the cloud process is dominated by homogeneous freezing, adding INPs will decrease ice cloud optical depth and likely induce a cooling effect because ice clouds (mostly cirrus) have a positive radiative effect<sup>64</sup>.



◀ Fig. 1 | **Climatologies and trends of aerosol parameters.** **a** | Left column: climatological spatial distribution of aerosol optical depth (AOD) calculated over 2010–2014 for black carbon, dust, organic carbon, sulfate, sea salt and all aerosols combined. The numbers at the top right indicate the global mean value. Middle column: as in the left column but for single-scattering albedo (SSA)<sup>71</sup>. Right column: as in the left column but for extinction-weighted aerosol layer height, calculated as a weighted average of the height of all layers using the total extinction of each layer as the weight (TABLE 1). **b** | Top row: linear AOD trends calculated over 2002–2016 (left) and changes in AOD by 2100 relative to 2014 for Shared Socioeconomic Pathway (SSP) 126 (middle) and SSP 370 (right) using the average of 14 Coupled Model Intercomparison Project Phase 6 models<sup>210</sup>. Values in the top right of each panel indicate the globally averaged trend or change. Bottom: as in the top row but for SSA. Together, these data provide an understanding of the sources, distributions, optical properties and trends of aerosols.

Absorbing aerosols can interact with clouds through the semi-direct effect, which refers to the heating of the ambient atmosphere, changing the temperature profile<sup>13,34</sup>. The sign of this effect depends on the relative height of the aerosol and cloud layer, as well as cloud type. BC near low clouds causes the most warming, whereas BC below clouds or near high clouds can lead to a cooling effect<sup>34,67</sup>. Overall, the majority of the latest climate models show a cooling effect by cloud adjustment in response to BC forcing. This cooling is due to the heating in the upper troposphere by BC, which decreases upper-troposphere stability, decreases high-level clouds and increases low-level clouds<sup>67–69</sup>. BC internally mixed with sulfate or organic aerosols might decrease or prevent the activation of these particles to form cloud droplets<sup>70</sup>.

### Measurement of aerosol properties

Measurements are fundamental in investigating the role of aerosols in the climate system. Since the year 2000, aerosol observations from instruments on the surface of Earth and in space have greatly expanded. The observations have provided crucial data to understand aerosol optical and microphysical properties, space–time variability and climate effects<sup>71–74</sup>.

**Aerosol measurement techniques.** Aerosol observation can be generally divided into in situ, surface-based remote sensing and space-borne remote sensing. In situ observations that sample the ambient air can accurately measure the mass concentration, scattering and/or absorbing properties, and more detailed information such as chemical composition, shape, mixing states, hygroscopicity and particle size distribution that determine CCN concentration<sup>75–77</sup>. When instruments are deployed on aircraft or tethered balloons, the vertical distribution of these properties can also be measured<sup>78</sup>. Due to their high accuracy and comprehensiveness, in situ measurements often serve as benchmarks for remote-sensing observation and model simulations<sup>7</sup>.

Remote-sensing instruments, which measure the transmitted and/or scattered radiances that contain the scattering and absorption characteristics of aerosols, are relatively easy to operate, albeit at the cost of decreasing the measurement accuracy and properties retrieved compared with in situ measurements. From the surface, the total column loading of aerosols (aerosol optical depth (AOD), TABLE 1) can be inferred from the attenuation of direct solar radiation from the

top of the atmosphere to the surface. Combined with diffuse radiation measured at multiple angles and spectral bands, different inversion algorithms have been developed to retrieve column-averaged aerosol SSA, phase function and size distribution<sup>79–81</sup> (TABLE 1) at moderate accuracy (for example,  $\pm 0.03$  for SSA), provided there is sufficient aerosol loading (typically AOD at 440 nm  $> 0.4$ , but also depending on surface brightness and variability)<sup>82</sup>. NASA has operated a global surface network using sky-scanning photometers configured in this fashion — the Aerosol Robotic Network (AERONET)<sup>71</sup>, which has now grown to over 800 sites covering many aerosol source regions. The climatologies of aerosol retrievals from AERONET<sup>26</sup> provide important quantitative insights into the magnitude and spectral variability of aerosol SSA and particle size distribution for different types of ambient aerosol. There are also similar regional Sun photometer networks, such as the SKYNET in Asia and Europe<sup>83</sup> and CARSNET in China<sup>84</sup>, that offer detailed information of regional aerosol optical properties.

Aerosols can also have complicated vertical distributions, with various profiles or layered structures of different types and sizes<sup>85,86</sup> (Supplementary Fig. 1). Lidars that emit a laser beam and measure the backscattered light can obtain such vertical information. For the simplest backscatter lidar, the extinction profile can be retrieved only by assuming an extinction-to-backscatter ratio<sup>87</sup>. Profiles of aerosol scattering/absorption and some particle size information can be retrieved using more advanced approaches, such as the multi-wavelength Raman scattering or high-spectral-resolution techniques, or a combination of backscattering lidar and Sun photometers<sup>88</sup>. Examples of established lidar networks include MPLNET (Micro-Pulse Lidar Network), which operates over worldwide locations<sup>89</sup>, and EARLINET<sup>90</sup> (European Aerosol Research Lidar Network) and LALINET<sup>91</sup> (Latin American Lidar Network), which operate in Europe and Latin America, respectively. A more comprehensive understanding of aerosol properties within a single column can be estimated by combining passive Sun photometers and active lidar<sup>92</sup>.

Knowledge of global aerosol variability generally relies on the analysis of global satellite measurements in combination with constraints provided by global aerosol models. For passive satellite sensors that measure solar radiation scattered back to space by the Earth–atmosphere system, the channels are typically located in the visible–near-infrared spectrum, from 400 to 900 nm, to optimize the detection of aerosols. After accounting for surface reflectance, molecular scattering and gas absorption, the angular spectral radiation received by a satellite sensor is a function of column AOD, column-averaged SSA and column-effective particle single-scattering phase function<sup>93</sup>. For single-view sensors, AOD is the primary parameter to be retrieved, and SSA and phase function are usually prescribed based on some prior knowledge of the global distribution of aerosol types<sup>72</sup>. Some particle size information, primarily fine and coarse mode fraction, can be inferred from the spectral dependence of AOD, but is only reliable over the ocean<sup>72</sup>.

Attempts have also been made to retrieve SSA from satellites. One approach is to use UV observations, based on the theory that the underlying surface is sufficiently dark, and that aerosol absorption can measurably change the spectral dependence of upwelling Rayleigh scattering by atmospheric gas<sup>94</sup>. This method has been applied to the Total Ozone Mapping Spectrometer and Ozone Monitoring Instrument data, and has achieved qualitative agreement with surface observations<sup>95</sup>. However, the UV technique cannot detect aerosols near the surface<sup>96</sup> and is highly sensitive to aerosol vertical distribution<sup>97</sup>. Another approach is through multi-angle viewing geometry, represented by the Multi-angle Imaging SpectroRadiometer, which can constrain SSA by separating the directional reflectance of the surface and aerosols<sup>98</sup>. This technique, if combined with polarization, can increase the sensitivity of SSA retrieval<sup>29,99,100</sup>. The superiority of this technique has been demonstrated in the analysis of SSA retrieved

by the Earth's first multi-angle polarization imager in space, the Polarization and Directionality of the Earth's Reflectance (POLDER)<sup>101,102</sup>, and by the Airborne Multiangle SpectroPolarimetric Imager<sup>103</sup>.

The vertical distribution of aerosols is difficult to retrieve from passive sensors and is usually prescribed in retrieval algorithms. The height of the absorbing aerosol layer can be detected using UV<sup>104,105</sup> radiance, near-UV polarimetry<sup>106</sup> or oxygen A or B band absorption<sup>107–109</sup> techniques under favourable retrieval conditions. The height of near-source wildfire, volcano and dust aerosol plumes can be derived geometrically and mapped from the parallax of plume contrast features as observed in multi-angle imagery<sup>110</sup>. However, active space-borne lidar is the only reliable method to obtain global information of aerosol vertical profiles on large scales, albeit with limited areal coverage. The only current space aerosol lidar in operation, Cloud-Aerosol Lidar with Orthogonal Polarization (CALIOP), is a two-channel

Table 1 | Definitions, meaning and radiative effects of some basic aerosol optical and microphysical properties

Variable	Definition	Physical meaning	Relevant radiative effect
Aerosol optical depth (AOD, $\tau$ )	The integration of aerosol extinction coefficient ( $\beta_e$ ) from the top of atmosphere to the surface	Quantity of direct solar radiation prevented from reaching the ground by the total column aerosol loadings	Direct effect
Spectral single-scattering albedo ( $\omega$ )	The ratio of scattering coefficient ( $\beta_s$ ) to $\beta_e$	How absorptive and reflective aerosols are	Direct effect and semi-direct effect
Phase function ( $P(\cos(\Theta))$ )	The radiance intensity at a certain direction $\Theta$ relative to the integral scattered radiance at all angles	The dependence of scattered radiance on scattering angle ( $\Theta$ ), representing which direction aerosols scatter the light	Direct effect
Polarized phase function ( $q_s(\Theta)$ )	The parameter in the scattering phase matrix to describe the change of polarization of light being scattered	The polarization properties of scattering light, which is sensitive to aerosol size distribution and complex refractive index	Direct effect and indirect effect
Asymmetry factor ( $g$ )	The integration of $P(\cos(\Theta))$	The proportion of forward scattering	Direct effect
Size distribution	A function that describes the relative amount of particles in each bin of size	Scattered radiance intensity is directly affected by particle sizes	Indirect effect
Effective radius ( $r_{\text{eff}}$ )	A weighted mean of the size distribution of aerosol particles	Simplifies the expression of aerosol distributions, which is useful for intercomparisons of different aerosols and their retrieval	Indirect effect
Extinction Ångström exponent, $\alpha$	An indicator describing how extinction AOD depends on the wavelength of the light	A qualitative indicator of aerosol particle size distribution. Typically, larger particles induce lower $\alpha$ . Also for direct forcing spectral dependence	Direct and indirect effect
Scale height ( $H_p$ )	The distance over which aerosol concentrations decrease exponentially	The vertical distribution is also important for assessing aerosol transports and material fluxes	Direct effect and indirect effect
Hygroscopic growth factor ( $f_b(\text{RH})$ )	The ratio of the wet particle diameter $D(\text{RH})$ at a certain relative humidity to the corresponding dry diameter $D(\text{dry})$	Determines the hygroscopic properties of aerosol particles and their influences, needed for cloud condensation nuclei behaviour and to interpret ambient AOD measurements	Direct and indirect effect
Extinction-weighted aerosol layer height	A weighted mean of aerosol layer height using the extinction of each layer as the weight	It is a proxy of aerosol vertical distribution/profile	Direct, semi-direct and indirect effect

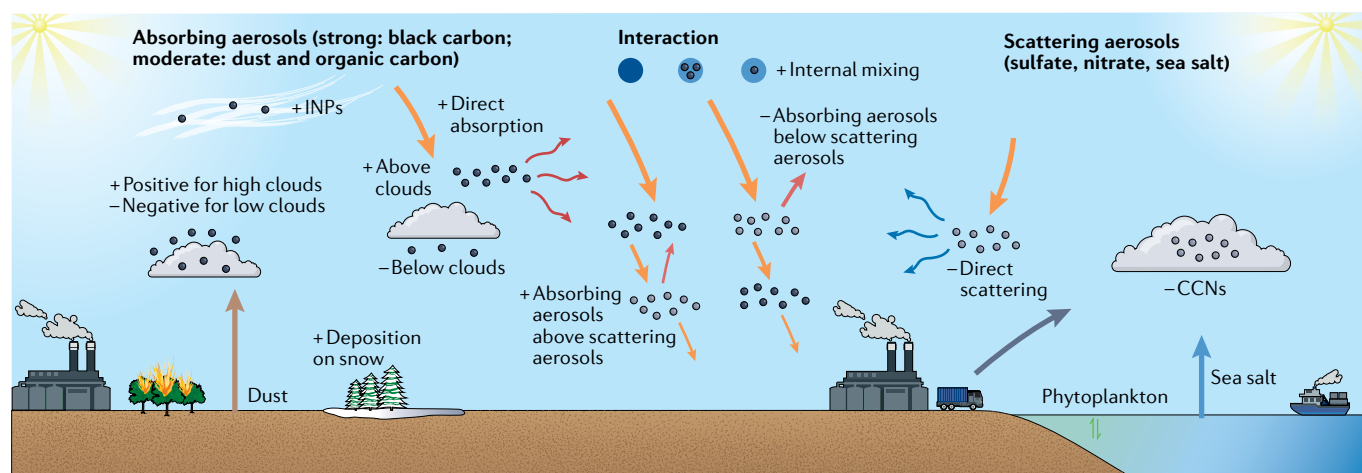


Fig. 2 | **The radiative effects of aerosols.** Schematic of radiative effects of absorbing (dark grey dots) and scattering aerosols (light grey dots), as well as their interactive effects. Scattering aerosols induce negative forcing (–) by directly reflecting sunlight and interacting with clouds; absorbing aerosols, in general, have a warming effect (+), although their interaction with clouds might produce slight cooling. The interaction between scattering and absorbing aerosols enhances the absorption and, thus, the warming effect. Light orange arrows represent incident sunlight; dark orange, scattered radiation by scattering aerosols; red, the radiation re-emitted by absorbing aerosols; and dark blue, scattered sunlight. CCN, cloud condensation nuclei; INPs, ice-nucleating particles.

backscattering lidar. By assuming the lidar ratio, it has the capability to derive aerosol extinction profiles from backscatter measurements, and some information about aerosol type based on depolarization sensitivity, surface type and prior knowledge of aerosol type from surface measurements<sup>73</sup>. The previous Cloud-Aerosol Transport System lidar<sup>111</sup> that was deployed on the International Space Station demonstrated the capability of diurnal sampling of clouds and aerosols<sup>112</sup>.

**Limitations of current aerosol observations.** For each type of observation, there is a trade-off between accuracy, comprehensiveness and spatial representation. To constrain ARI, AOD, spectral SSA, the phase function and their vertical distribution are needed. In particular, both AOD and SSA need to be measured at an accuracy of  $\sim 0.01$  to yield a global mean aerosol direct forcing uncertainty comparable with that of GHGs<sup>11,31,113</sup>. More detailed information is needed to constrain aerosol–cloud interaction. Model estimations require particle hygroscopicity and high-resolution size distribution (TABLE 1) down to sizes that cannot be distinguished with remote sensing alone<sup>114</sup>. For observational-based estimates, some proxies for aerosol size, such as aerosol index (AOD multiplied by the Ångström exponent), have been considered<sup>115</sup>.

In situ observations are the only means to measure the complete set of parameters at the required accuracy to constrain aerosol forcing. For example, in situ instruments can measure aerosol scattering at an accuracy below 10% (REF. 116) and absorption at an accuracy below 20% (REFS 117,118). For the information needed to estimate aerosol–cloud interaction, surface and aircraft platforms must be jointly deployed so that the horizontal and vertical distributions of aerosol size distribution, chemical composition and cloud microphysical parameters are accurately measured. However, some large particles

and INPs are still difficult to measure with the current in situ technique<sup>119</sup>. Notably, in situ measurements typically sample only over a few metres in the vicinity of the instrument. Column-integrated or averaged values of some aerosol parameters can be relatively well retrieved under clear sky conditions; however, certain assumptions must be made, and only the AOD retrieval can meet the required accuracy ( $\sim 0.01$ ). Knowledge of the aerosol vertical distribution offered even by active remote sensing is mostly limited to extinction, with weaker constraints on scattering and absorption properties. Furthermore, the most obvious drawback of in situ or surface remote sensing is the lack of global coverage, particularly for quantities that vary on large spatial scales. Also, the maintenance and calibration of instruments differs by site, creating problems in integrated usage of observations from different instruments.

Although satellite remote sensing can overcome the spatial coverage and calibration limitations, it has additional sources of uncertainty compared with surface observations. The most reliable parameter retrieved quantitatively is AOD; however, existing sensors can only achieve an accuracy of  $\sim \pm 0.02 \pm 20\%$  of the AERONET AOD for a large-scale average<sup>72</sup>, insufficient by itself to constrain aerosol forcing. It is difficult to retrieve SSA to the accuracy needed to constrain aerosol forcing, due to its high sensitivity to surface noise, even with current multi-angle polarization designs. The accuracy of the aerosol extinction profile retrieved from space lidar depends on the assumed lidar ratio, which is prescribed according to limited surface and in situ observations and is significantly impacted by aerosol absorption<sup>73</sup>. The vertical distribution of absorbing aerosols and SSA cannot be retrieved quantitatively with satellite remote sensing.

In short, on a global scale, current remote-sensing observational techniques can only retrieve aerosol

loading properties, such as AOD and the extinction profile, with moderate confidence, and the accuracy of aerosol microphysical properties retrieved by remote sensing alone is not adequate to constrain aerosol forcing to a level comparable with GHGs. The most critical factors, especially quantitative spectral SSA and its vertical distribution, are only available through limited in situ aircraft observations.

### **Climatology and temporal changes**

Because of the short aerosol lifetime, the spatial distribution of different aerosol types is highly heterogeneous. Aerosol concentration over different regions also exhibits short-term or long-term variability, produced by temporal changes of emissions, meteorological and climate conditions, and some extreme events.

**Climatology of aerosol distribution.** According to the Coupled Model Intercomparison Project Phase 6 (CMIP6) model results, most aerosols are concentrated near their sources, which results in their highly variable horizontal and vertical distribution (FIG. 1). Sulfate aerosols are concentrated over East and South Asia, where anthropogenic emissions are the most intense. These two regions also exhibit high BC and organic carbon concentrations, together with South America, Southern Africa and Southeast Asia, where biomass-burning-related BC and organic carbon emissions can be intense<sup>120</sup>. Dust distributions emanate from deserts in North Africa, the Middle East and Central Asia, and extend to their surrounding areas. Sea salt is concentrated over the oceans. The SSAs at mid-visible wavelength for dust, organic carbon and sulfate are typically around 0.97 at most wavelengths; sea salt has SSA essentially equal to 1. Although the simulated SSA for BC is below 0.2 (FIG. 1), such low SSA cannot be observed as BC is typically mixed with the other species. These aerosol species combined yield relatively low SSA values found over East and South Asia, Southern Africa, Southeast Asia and southern South America compared with other regions (FIG. 1). The vertical distribution is expressed as the extinction-weighted height (EWH, TABLE 1), which represents the layer that contributes the most to column AOD. Overall, the EWH is lower near sources than remotely, which is reasonable, as elevated aerosols typically travel longer distances. The EWH at emission is the lowest for sea salt and the highest for BC and organic carbon over biomass-burning regions and for volcanic emissions. Nonetheless, uncertainties in the above parameters can be considerable. For example, over high-aerosol-concentration regions such as North Africa and East Asia, the spread in AOD can be as large as 50% (Supplementary Fig. 2).

**Temporal changes of aerosol scattering and absorption properties.** To understand the role of aerosols in climate change, it is necessary to monitor long-term changes in aerosol amount and optical properties. Statistically significant AOD trends since the late 1990s have been found in different parts of the world based on satellite retrievals, with declines of  $\sim 0.01 \text{ year}^{-1}$  over eastern USA, western Europe and the tropical North Atlantic, strong

increases of  $0.02 \text{ year}^{-1}$  over the Arabian Peninsula and weak increases of  $\sim 0.01 \text{ year}^{-1}$  over East China and the Indian subcontinent<sup>121,122</sup>. Since  $\sim 2006\text{--}2008$ , AOD over East Asia also began to decrease<sup>123</sup>, leaving the Indian subcontinent and the Arabian Peninsula as the only regions with significant upward AOD trends (FIG. 1).

However, fewer results are available for SSA trends due to the lack of consistent, global observations. Limited SSA retrievals from surface Sun photometers indicate that SSA has systematically increased by as much as  $0.03 \text{ decade}^{-1}$  at sites in North America, Europe and Northeast Asia from 2000 to 2013 (REF.<sup>124</sup>). Updated records from AERONET still indicate statistically significant SSA increases over most European, North American, African and Asian sites (FIG. 1). These SSA changes are of great importance for both the global radiation balance and satellite retrievals. In particular, a trend in aerosol SSA will affect the accuracy of any trend in AOD retrieved if SSA is assumed constant<sup>125,126</sup>, which is the case in many passive satellite aerosol-retrieval algorithms.

**Insights on the change of aerosol properties during the COVID-19 lockdown.** The lockdown induced by the COVID-19 pandemic serves as a valuable opportunity to examine the effect of strict emission control measures that could take place in the future<sup>127</sup>. During the pandemic, extensive lockdown was implemented worldwide, which dramatically reduced the emission of anthropogenic aerosols and weakened their direct and indirect radiative forcing<sup>128,129</sup>. Over East Asia, anthropogenic aerosol emissions decreased by 32%, resulting in an increase of surface shortwave radiation of  $1.3 \text{ W m}^{-2}$  (REF.<sup>130</sup>). Along with the decreased total aerosol loading, changes in aerosol composition, and, thus, their optical properties and radiative effects have also been observed. In particular, absorbing carbonaceous aerosols experienced the most significant reduction in Asia (by 48–70%)<sup>131</sup> and Europe (by 20–40%)<sup>132</sup>, whereas secondary aerosols that are mostly scattering even increased due to the increase in tropospheric  $\text{O}_3$  associated with the reduction of  $\text{NO}_x$  emissions. Specifically, a 65% reduction of  $\text{NO}_x$  during the lockdown has been observed in East China, making the atmospheric oxidizing capacity at the peak of secondary aerosol formation and increasing  $\text{O}_3$  production by as much as 100% (REF.<sup>133</sup>). Specifically, the combined effect was an increase in the reflectivity of aerosols or increased SSA<sup>134</sup>. Although the aerosol forcing induced by these short-term perturbations is minor compared with the baseline condition<sup>135</sup>, this extreme case provides insights into future changes of aerosol scattering and absorption under different economic growth scenarios.

### **Future projections of the change of aerosol properties.**

Global and regional aerosol concentrations and their optical properties might substantially change in the future. On one hand, emission-intense countries, such as China and India, have implemented or will likely implement stricter air quality control regulations in an effort to alleviate air pollution, resulting in an overall decrease in AOD (FIG. 1). Anthropogenic aerosols have already decreased markedly in China since 2008, with a



## Box 1 | Modelling of aerosol radiative and climate effects

**Zero-D models**

The most straightforward, intuitive effect of aerosols on the climate system is a change in the planetary albedo, whose first-order effect can be estimated using the zero-D model by considering the Earth as a spherical blackbody as a whole.

The impact of aerosols is reflected in the change of planetary albedo. For a clear sky, aerosols can induce positive or negative changes in  $A$  that correspond to negative or positive changes in Earth's temperature, respectively, depending on aerosol single-scattering albedo (SSA) and surface reflectance. Under a cloudy sky, the aerosol impact on cloud albedo also needs to be estimated. The impact is usually positive but can be negative for regions with a large fraction of absorbing aerosols or low SSA. However, the simple zero-D model cannot provide estimates of surface climate or reflect the dependence of aerosol forcing on its vertical distribution.

**1-D models**

Because of the limitations of zero-D models, they have been extended to column radiative transfer models, in which the aerosol parameters, including aerosol optical depth, SSA, phase function or asymmetry parameter  $g$  (TABLE 1) are prescribed for each layer. By comparing the radiative flux at the top of the atmosphere or the surface with and without aerosols, aerosol radiative forcing (ARF) can be calculated. The effect of clouds can also be accounted for by parameterizing their optical properties. These models work well for sensitivity experiments but are not suitable for global analyses.

**General circulation models**

Aerosol modules are thus incorporated into general circulation models (GCMs) to investigate their impact on global climate. Early GCMs usually adopted an offline approach, whereby the aerosol mass density fields were simulated using a chemical transport model. Then by assuming complex refractive indices, size distributions and hygroscopic growth factors for each species, their masses were converted into optical properties that participate in the radiative transfer calculation. The chemical transport model models the emission, chemical reaction and gas-to-particle conversion, transport, and dry and wet deposition processes of different aerosol species, and can be driven by the GCM simulated meteorology fields or by reanalysis meteorology. This configuration allows aerosols to influence radiation and dynamics in the model, but the aerosol processes are not interactive with the dynamics.

New-generation GCMs are mostly two-way coupled, in which the chemistry module is driven by the simulated meteorology and the calculated aerosols feed back to the radiation and dynamics for each model step. Both the impact of aerosols on climate and the impact of climate on aerosols are simulated in this way. The global ARF is typically estimated as the difference between the top of the atmosphere or tropopause net flux simulated using present-day aerosol emissions and that using pre-industrial aerosol emissions (usually for the year 1750).

**Earth system models**

The newest global models — global Earth system models — incorporate many real-world processes beyond the general circulation, such as those associated with vegetation, sea ice and land ice. Aerosols are mostly also interactive in the Earth system models. More realistic ARF estimations can be achieved using these models, as well as estimations of the impact of aerosols on many regional and global physical processes.

0.2 decade<sup>-1</sup> downward AOD trend<sup>136</sup>, a decrease that will likely continue. Aerosols in South Asia are projected to decrease at least around 2050 and could be reduced by as much as 50% by 2100 (REF. 137). On the other hand, emissions might shift to currently underdeveloped regions of Africa, Central and South America, and Southeast Asia, especially under the Shared Socioeconomic Pathway (SSP) 'regional rivalry' scenario (SSP3)<sup>137</sup>. Emission of natural aerosols, such as dust, biogenic aerosols formed from biogenic organic vapours, and BC and organic carbon aerosols from wildfires, also seem likely to increase due to the increase of dry and hot extremes and the increase of wind speed under global warming<sup>138–140</sup>. Sea-salt aerosol emission tends to increase with a warmer ocean surface<sup>141,142</sup>, although the amount might be small and varies in different models<sup>4,143,144</sup>.

More importantly, changing anthropogenic and natural emissions alter not only total aerosol loading but also aerosol optical properties, such as SSA. For example, with the adoption of clean energy as predicted by SSP<sup>145</sup> experiments, the fraction of absorbing aerosols is likely to decrease, which means an increase of SSA (FIG. 1). However, increased wildfire emissions<sup>131</sup> means that more light-absorbing aerosols might be released, leading to a darkening aerosol effect regionally<sup>139</sup>.

In the future, it has been projected that aerosols might induce a negative radiative forcing up of to  $-0.09 \text{ W m}^{-2}$  due to increased aerosol concentration caused by reduced precipitation<sup>140</sup>. Dust aerosol alone can account for  $-0.04$ – $0.02 \text{ W m}^{-2}$  (REF. 146). Strict emission controls in polluted areas such as China imply a possibly weakened projected forcing by anthropogenic aerosols, which then positively contributes to future warming because well-mixed GHGs will continue to increase<sup>147,148</sup>. However, there is little confidence about how SSA and its impact on the projected forcing will change in the future, leaving a large uncertainty for climate prediction.

**Aerosol radiative and climate effects**

There have been many attempts to quantify the different effects of aerosols, as well as their impacts on global and regional climate<sup>8</sup>. This section summarizes progress in these areas and discusses the remaining uncertainties.

**Estimating aerosol radiative forcing.** Aerosol radiative forcing (ARF) can be estimated readily using interactive chemistry–climate models by comparing the radiative fluxes calculated using present-day and pre-industrial aerosol emissions (BOX 1). Many projects have been carried out to intercompare the ARF estimated by different models, such as the CMIP<sup>149</sup>, AeroCom<sup>150</sup> and ACCMIP<sup>151</sup> projects. The inter-model ARF spread is often presented as its uncertainty<sup>4</sup>, although it actually represents model diversity, which is generally a lower bound on uncertainty.

Global ARF has also been estimated purely from satellite observations. The direct forcing is easier to estimate, which is based on constructing the relationship between anthropogenic AOD (sometimes taken as fine particles, though this does not account for natural biomass burning, sulfate, secondary organic and biogenic particles, nor for the fine-particle part of the dust and marine particle size spectrum) and radiative flux, using collocated radiation and aerosol retrievals by satellites<sup>152</sup>. However, this estimate is confined to clear-sky conditions, which leads to an overestimate of the overall negative forcing, and also neglects the positive forcing by absorbing aerosols above clouds. Estimation of cloudy-sky direct forcing requires the vertical profiles of both aerosol extinction and SSA, which is challenging. To estimate the forcing from aerosol–cloud interaction, the relationship between retrieved cloud properties (such as cloud reflectance, effective radius and liquid water content) and AOD<sup>153</sup> or more precise aerosol proxies<sup>115,154</sup> needs to be established. However, the cloud and aerosol properties are typically from nearby but different pixels, as cloud and AOD retrievals cannot

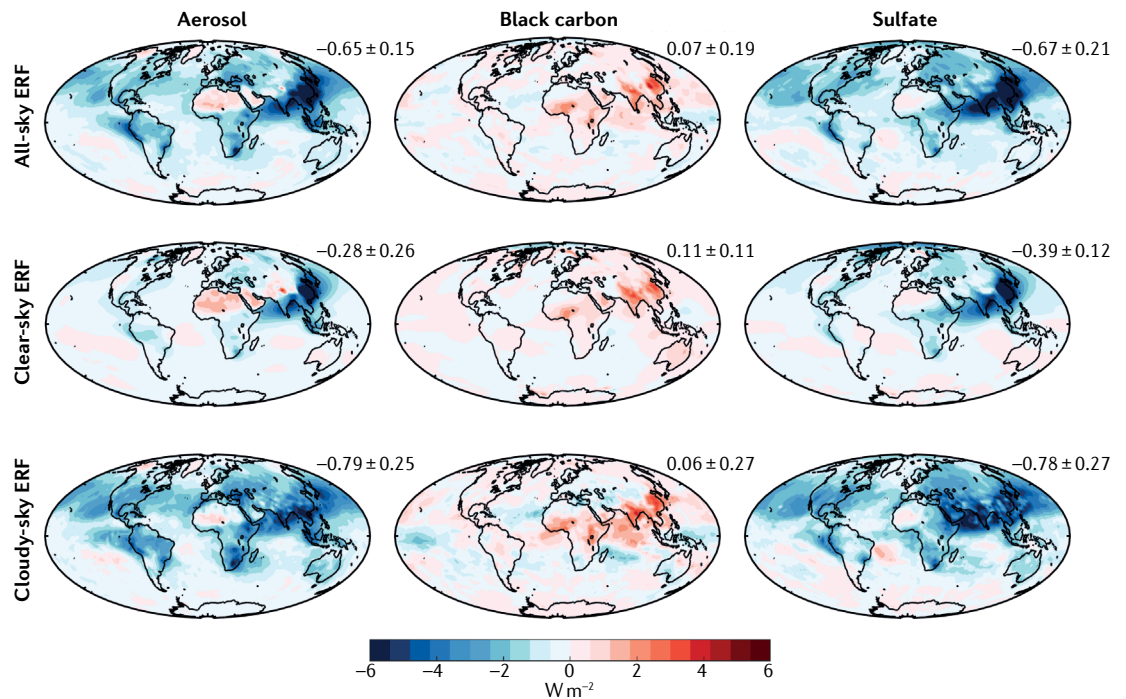


Fig. 3 | **Effective radiative forcings for all aerosols, black carbon and sulfate over 1850–2014.** Top row: all-sky effective radiative forcing (ERF) for all aerosols (left), black carbon aerosols (middle) and sulfate aerosols (right). ERF is calculated by averaging the results of 14 Coupled Model Intercomparison Project Phase 6 models as the difference in the net top of the atmosphere radiative flux between the aerosol forcing run for the year 2014 and the pre-industrial control run. The numbers at the top right represent the multi-model mean and standard deviation. Middle row: as in the top row but for clear-sky ERF. Bottom row: as in the top row but for cloudy-sky ERF. The climate forcings of scattering (sulfate) and absorbing (black carbon) aerosols are opposite over most regions, and that of absorbing aerosols is highly uncertain.

be strictly collocated, which creates uncertainty in the results. The effective radiative forcing for aerosols (ERF) includes aerosol–radiation interaction (ERF<sub>ari</sub>) and aerosol–cloud interaction (ERF<sub>aci</sub>) effects, and allows shorter-timescale atmospheric elements to adjust to equilibrium. Observation-based ERF<sub>ari</sub> is slightly larger than model-based ERF<sub>ari</sub>, whereas the ERF<sub>aci</sub> estimated by the two approaches largely converge (IPCC AR6)<sup>4</sup>. In particular, applying the decomposition method that separates ERF<sub>aci</sub> into instantaneous forcing and rapid adjustments appears to improve the convergence of model and observation-based ERF<sub>aci</sub><sup>155</sup>.

**Aerosol radiative forcing and its uncertainties.** The strongest aerosol forcing is found in the Northern Hemisphere, primarily in the mid-latitudes, where most anthropogenic aerosol emissions are concentrated (FIG. 3). The largest negative forcing, reaching below  $-5 \text{ W m}^{-2}$ , is found over East Asia. Positive forcing mostly occurs over the desert regions, including northwest China, the Sahara and the Middle East, due to the high surface albedo. The forcing of BC and sulfate is representative of most absorbing and scattering aerosols, respectively, except where iron oxide absorption from mineral dust particles dominates. The sign of the forcing is mostly positive for BC but negative for sulfate, especially over land. The all-sky forcing is nearly three times as much as the clear-sky forcing based on these

simulations. Considering that all-sky ERF<sub>ari</sub> is typically smaller than that under clear sky, the more negative all-sky forcing indicates a significant contribution from ERF<sub>aci</sub>. However, the BC forcing is more negative for all-sky than clear-sky conditions over the ocean, implying negative forcing from the cloud adjustments to BC forcing. Note that the spread in the ERF among different models can be considerable (Supplementary Fig. 3), indicating large uncertainty.

Over the past 20 years, numerous attempts have been made to estimate different components of aerosol forcing based on observation, modelling or both (FIG. 4 and Supplementary Tables 1,2). Earlier observation-based estimates gave more negative direct forcing under clear-sky conditions but reached consistency with model estimates at  $\sim -0.7 \text{ W m}^{-2}$  after about 2007, driven largely by global, monthly satellite AOD products. All-sky direct forcing is estimated at about half as large as clear-sky direct forcing, as cloud scattering significantly masks the scattering of aerosols. The estimated magnitude stays relatively stable after 1995, varying between  $-0.5$  and  $0 \text{ W m}^{-2}$ , with four estimates after 2020 arriving at  $\sim 0.25 \text{ W m}^{-2}$  (FIG. 4b and Supplementary Table 1). The indirect forcing estimates exhibit greater uncertainty and more fluctuation over time, although the smaller effects in earlier estimates are associated with calculations of only the albedo effect. The latest model-based estimation indicates an indirect forcing of  $\sim -0.75 \text{ W m}^{-2}$ , which is slightly weaker than the IPCC AR6 result that

combines model and observations<sup>4</sup>. There are far fewer estimates of the semi-direct effect of absorbing aerosols than the direct and indirect effects. The mean values of different reported estimates fluctuate between  $-0.5 \text{ W m}^{-2}$  and  $+0.2 \text{ W m}^{-2}$ , with large error bars. This effect, however, is likely a minor contribution based on current understanding<sup>4</sup>.

An encouraging result is the decrease in uncertainty estimates of the direct aerosol forcing over time (FIG. 4a,b), especially for the all-sky direct radiative forcing, which tends to stabilize with an uncertainty of  $\sim \pm(0.1-0.4) \text{ W m}^{-2}$ . The indirect forcing uncertainty is still large, reaching or exceeding 100%. Large uncertainty is also present in estimates of the semi-direct effect (FIG. 4e and Supplementary Table 2). Limited global estimates indicate an averaged negative forcing in the range of  $-(0.4-0.1) \text{ W m}^{-2}$ . Yet, the uncertainty can well exceed the mean and change the forcing to weakly positive.

Different methods are used to estimate the uncertainty of different forcing components, meaning that reported uncertainties might not be directly comparable. In particular, many model-based estimates consider the multi-model spread (or the model diversity) as the uncertainty, which is likely to underestimate model uncertainty, especially as model intercomparison projects encourage modellers to adopt similar assumptions. Overall, consensus about the total aerosol forcing uncertainty shows some decrease over time<sup>9</sup>. However, substantial differences still exist, especially for the aerosol–cloud interactions.

Sensitivity experiments indicate that uncertainties in SSA and the vertical distribution of absorbing aerosols contribute the most to the uncertainty of direct forcing. In particular, a  $\pm 0.03$  uncertainty in SSA, which is already the lower uncertainty limit of surface remote sensing, can contribute 50% of the total direct forcing uncertainty<sup>11</sup>. The vertical distribution of absorbing aerosols can also contribute to  $\sim 10-20\%$  of the direct forcing uncertainty globally. With respect to modelling, the assumed aerosol mass extinction and absorption efficiencies, which are needed to convert the simulated aerosol mass into optical properties, show large variations among different models but are poorly constrained by observations<sup>7</sup>.

Uncertainty in the aerosol indirect effect can be associated with both the lack of understanding of aerosol and cloud microphysical processes (such as precursor emissions, chemical reactions, nucleation and growth and hygroscopicity), incorrect/coarse representation of these in models, and the role of transport and transformation processes. For example, models disagree in characterizing the differences in the aerosol size distributions between present-day and pre-industrial conditions, and mixing states of absorbing and scattering aerosols, which leads to different AOD, CCN concentrations and cloud optical properties. Aerosol vertical distribution determines the involvement of aerosol in cloud processes but is poorly constrained. Moreover, microphysical processes in ice or mixed-phase clouds are very unclear. The role of different INP types, in particular, BC as an INP, is debated but not yet well constrained by observations. Competition between homogeneous freezing

and heterogeneous nucleation before adding aerosol particles might lead to opposite final forcing estimates<sup>64</sup>.

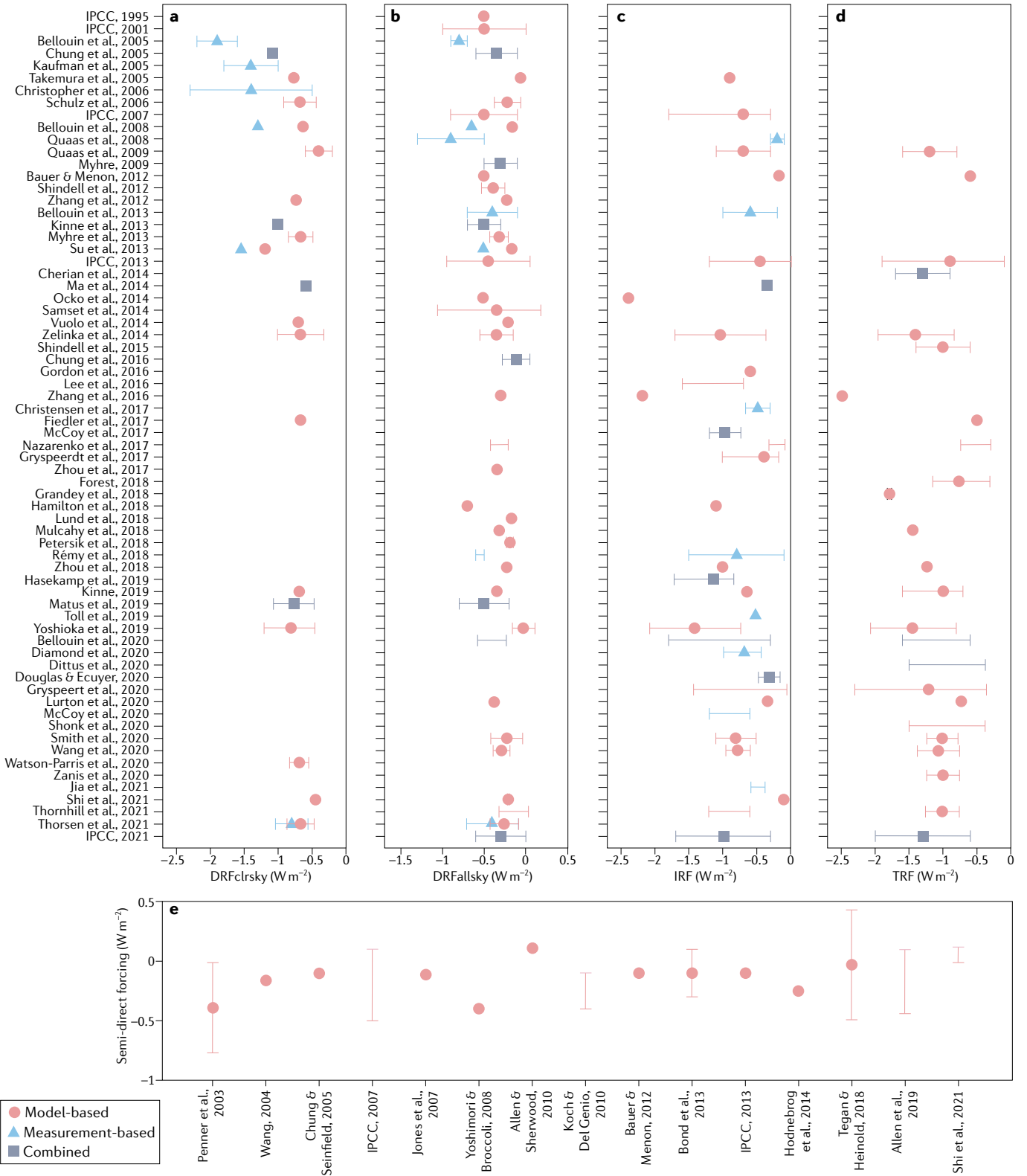
The uncertainty in semi-direct aerosol forcing arises mainly from the vertical distribution of BC and sometimes the cloud water content. A negative forcing is produced below a relatively high BC layer, which causes a cooling and an increase of low-level clouds. However, the BC loading in the upper troposphere in models might be biased high compared with observations<sup>156</sup>, and, so, could be responsible for the simulated negative forcing.

Knowledge of pre-industrial aerosols is also critical in estimating anthropogenic contributions to aerosol forcing. Different estimates of pre-industrial aerosol emissions can lead to 15–60% variability in aerosol forcing estimate<sup>157</sup> and contribute to  $\sim 45\%$  of the total aerosol forcing uncertainty<sup>158</sup>. However, pre-industrial aerosol concentration cannot be measured and is, therefore, typically inferred from measurements in remote areas<sup>157,159</sup>, contributing further to forcing uncertainty<sup>160</sup>. Other external factors, such as in radiative transfer calculations, absorbing gas profiles, surface albedo and dynamical background, also contribute to the model-estimated forcing uncertainty<sup>161,162</sup>.

**Global climate impacts.** Although the largest concentrations of aerosols and their instantaneous forcing occur near their sources, their impact on the energy balance and climate can be more geographically extensive and profound. They introduce perturbations in the radiative energy balance at the top of the atmosphere and the surface, both of which are spatially inhomogeneous. The heterogeneous energy perturbation by aerosols includes a pronounced interhemispheric asymmetry that has particular implications for the climate in both hemispheres<sup>163–165</sup>. They directly change the atmospheric and oceanic circulation by altering the vertical and horizontal thermal structure on hemispheric scales. By inducing a sea surface temperature (SST) response similar in pattern but opposite in sign to that of GHGs<sup>166</sup>, aerosols might have contributed to the global warming slowdown from 2000 to 2015 (REF.<sup>167</sup>). The aerosol-induced SST changes further result in ocean circulation anomalies and can impact the Atlantic meridional overturning circulation<sup>168</sup>. In contrast to the GHG effects on climate, which tend to strengthen the hydrologic cycle, aerosols tend to weaken it<sup>148,169–171</sup>.

Aerosols also contribute to some large-scale climate anomalies, such as Arctic warming<sup>172</sup>, extreme Northern Hemisphere winters<sup>173</sup>, precipitation reduction in the Northern Hemisphere<sup>174</sup>, as well as hemispherically asymmetric rainfall trends<sup>175</sup>. In these effects, absorbing and scattering aerosols typically induce distinct changes in the global SST pattern<sup>176</sup>, energy budget<sup>177</sup>, hydrological cycle<sup>15</sup> and climate responses<sup>178</sup>.

**Regional climate impacts.** The local cooling or warming induced by aerosols can form a temperature gradient between polluted regions and the surrounding areas, which leads to a perturbation or shift in regional circulation. The most representative case is the monsoon scenario, especially in South and East Asia. Aerosol cooling



at the surface reduces the temperature contrast between land and ocean, weakening the South and East Asian monsoons<sup>171,179–181</sup>. The fraction of absorbing aerosols plays a critical role in the monsoon shifts<sup>182</sup>. BC mixed with organic carbon forms the so-called atmospheric brown clouds, first discovered over the Indian Ocean in air transported from the Indian subcontinent<sup>169</sup>.

These aerosols heat the atmosphere above the ocean, reducing the temperature gradient between ocean and land, and weakening the South Asian monsoon. BC can also substantially contribute to the weakening of the African and South American monsoons<sup>183,184</sup>. Both local and remote aerosols can affect regional changes in the hydrologic cycle in Asia<sup>185</sup>.

◀ Fig. 4 | **Aerosol radiative forcing and its uncertainty.** **a** | Published estimates of clear-sky direct radiative forcing (DRF<sub>clrsky</sub>) since 1995. **b** | As in **a** but for all-sky direct radiative forcing (DRF<sub>allsky</sub>). **c** | As in **a** but for indirect radiative forcing (IRF). **d** | As in **a** but for total radiative forcing (TRF), which includes aerosol–radiation interactions and aerosol–cloud interactions. **e** | As in **a** but for semi-direct forcing. Estimations of direct forcing converge over time, yet those of aerosol–cloud interaction and semi-direct effects still vary. Details on references for panels **a–d** are provided in Supplementary Table 1; details for panel **e** are provided in Supplementary Table 2.

On even smaller scales, aerosol cools the surface and increases the lower atmospheric stability. Absorbing aerosols are more efficient in this process, although the overall effect is usually larger for scattering aerosols due to their higher loading<sup>186</sup>. This process might decrease the planetary boundary layer height, resulting in the so-called aerosol–boundary-layer feedback<sup>187</sup>, a process thought to significantly contribute to severe pollution events in China<sup>37</sup>.

### Summary and future prospects

Aerosols are known to have an important role in the regional and global climate system. Tremendous efforts have been made, in both observation and modelling, to advance understanding of the mechanisms by which aerosols impact the climate system and to increase the accuracy of aerosol forcing estimates. Many physical processes through which aerosols impact the global atmospheric and oceanic circulation, and regional climate anomalies, have been identified. In terms of forcing estimation, some convergence has been achieved between model-based (bottom-up) and observation-based (top-down) results. Unfortunately, the discrepancies among different models are still considerable. The latest models still suggest an inter-model forcing spread of ~50% (REF.<sup>188</sup>), and the actual model uncertainties are probably larger. When the models are tuned to fit the observed historical increases in temperature, this large uncertainty also impacts climate sensitivity estimates, which translates into a large uncertainty in climate projections. As such, confidence is still low in quantifying the role of aerosols in the climate system.

There is now compelling evidence that human influence has warmed the atmosphere, ocean and land. Drastic reductions in global GHG emissions are required to keep the surface temperature increase within 2 °C by the end of the twenty-first century<sup>4</sup>. It is imperative to understand the aerosol component of climate change better so that the required constraints on GHG concentrations can be defined accurately. There is, thus, urgent need to improve understanding of the role of aerosols in the climate system.

The fraction of aerosol absorption relative to scattering, expressed as the SSA parameter, is one of the most critical factors in quantifying the role of aerosols in the climate system. Uncertainties in SSA as well as its vertical distribution contribute substantially to uncertainties in ARI. The fraction of scattering and absorbing aerosols also impacts aerosol–cloud interaction estimates. However, there is no consistent global monitoring of SSA, leaving this parameter poorly constrained in climate models, which leads to further uncertainties in aerosol forcing estimates. In addition, aerosol size distribution, or

a proxy of it, is critical in quantifying aerosol–cloud interaction. Better constraining pre-industrial and present-day aerosol SSA and size distribution from observations, and better representation of these in climate models, are, thus, warranted to quantify aerosol forcing.

**Future observation needs.** Future aerosol observation strategies focus on expanding the space of parameters that can be retrieved by satellite sensors and improving the measurement accuracy. For this purpose, high-accuracy, multi-angle polarization measurements could be a promising technique. NASA's Glory mission<sup>189</sup>, carrying the first high-accuracy polarimeter with the potential to produce a more nuanced picture of aerosols, unfortunately failed at launch. In 2018, China launched the country's first multi-angle polarimeter, the Directional Polarimetric Camera (DPC), with similar settings as POLDER, but it stopped service in 2020. AOD and the fine mode fraction over land have been retrieved from the DPC with reasonable accuracy<sup>86</sup>. Two other DPCs on different platforms will be launched between 2022 and 2026. NASA's HARP multi-angle, multi-spectral polarimeter imager was launched on a CubeSat in April 2020 (REF.<sup>190</sup>), and an updated version, HARP2, will be launched on NASA's Plankton, Aerosol, Cloud, ocean Ecosystem (PACE) space mission<sup>20</sup>. Two more advanced multi-angle polarimeters, the 3MI sensor by the European Space Agency<sup>18</sup> and the SPExone sensor on PACE, are both scheduled to orbit in the next two years. The increasing number of polarimeters and rapidly growing volume of polarimetric data, especially from orbital instruments, along with sustained advances in forward modelling, retrieval methodologies and algorithms, serve as a compelling reason to envision multi-angle polarimetry as the main tool for global aerosol monitoring and characterization<sup>19</sup>.

To derive the vertical distribution of more parameters, especially SSA, a multi-wavelength, hyperspectral resolution technique that isolates molecular scattering from aerosol scattering has been proposed, which can provide information on the profiles of aerosol extinction, absorption and size distribution<sup>191</sup>. The lidar-based technique has limited spatial sampling compared with imagers, but it promises to be implemented on satellite platforms, and many aircraft-based experiments have already been carried out<sup>21,181</sup>.

A combination of the above-mentioned multi-angle, polarized passive sensor and HSRL lidar, and possible multi-channel spectrometers, can yield invaluable insights into how different types of aerosols interact with radiation, clouds and the climate system. Multiple campaigns under NASA's Aerosol-Cloud-Ecosystems mission demonstrated the advantage of such combinations of sensors in retrieving horizontal and vertical variability of key aerosol parameters<sup>192</sup>. Several satellite platforms in development offer this configuration, including NASA's PACE mission<sup>193</sup>, Aerosol-Clouds, Convective-Precipitation mission<sup>194</sup> and Europe's EarthCARE mission<sup>195</sup>.

However, satellite remote sensing must be combined with in situ observations to reach the required accuracy of different parameters for constraining aerosol forcing

and to obtain key parameters that cannot be retrieved from remote sensing alone. Accurate measurement of key aerosol parameters likely requires the establishment of an international network with a routinely operating, relatively small aircraft in situ sampling programme that is designed to provide the key particle microphysical property information unobtainable or inadequately constrained by remote sensing for the major aerosol air masses identified by chemical transport models<sup>17</sup>. Such data would improve both model and satellite-retrieval assumptions about particle size distributions and CCN properties, hygroscopicity, SSA, as well as the mass extinction efficiencies used to relate satellite-derived AOD to aerosol mass in climate and air quality models. Information optimization techniques can be used to select sites where the measurements can contribute the most to reducing forcing uncertainty<sup>187</sup>. Urgently needed are highly accurate and efficient retrieval algorithms designed in line with future satellite sensors, as well as data synergy techniques that maximize the information of multi-sensor datasets and in situ observations.

Given the difficulty of simulating all aerosol–cloud interactions, reliable determination of the ERF<sub>aci</sub> requires global monitoring of aerosol and cloud properties. Planetary missions have demonstrated the ability of a high-accuracy (~0.1%) polarimeter to obtain accurate microphysical data such as refractive index and size distribution on aerosols and cloud-top particles. A second instrument — a Michelson interferometer that simultaneously measures the spectrum of heat radiation emitted by Earth at the same spatial resolution as the polarimeter — can provide water vapour, ozone and temperature in several layers of the atmosphere, as well as cloud-top temperature and cloud properties to a greater depth than that reached by the polarimeter. Along with a simple high-resolution camera, these two instruments on a small satellite would provide a monitoring capability crucial to help understand aerosol–cloud interactions<sup>196</sup>. Such remote sensing must be complemented with intensive aircraft field campaigns aimed at better characterizing the microphysical processes involved in aerosol–cloud interactions, so that parameterizations of these processes in models can achieve greater accuracy.

**Future modelling needs.** Constraining ARI in models requires accurate simulation of the emissions (including primary aerosols and the precursor gases for secondary aerosols), chemical reactions, particle growth, transport and removal, as well as the optical and microphysical properties of different aerosol species. It is necessary to take advantage of different types of observations, especially the advanced sets of satellite and in situ observations envisioned in the previous subsection, to improve the representation of aerosol extinction, absorption, size distribution, mixing and other related processes in climate models. Data assimilation techniques have been extensively used that not only assimilate AOD<sup>197</sup> retrievals but also aerosol absorption<sup>198</sup> and SSA retrieved by POLDER<sup>199</sup>, and aerosol extinction profiles retrieved by CALIOP<sup>200,201</sup>. These practices effectively improved simulation results, yielding several global aerosol reanalysis datasets<sup>202,203</sup>. Nonetheless, the retrieved products

themselves rely on model assumptions and their uncertainties will negatively affect the assimilation results. A comparison of the radiances derived with assimilated aerosol properties and those observed by satellites can test some of the assumptions of aerosol microphysical properties between the model and the retrieval algorithm for inconsistency. Such practices will facilitate the interpretation of the measurements and possibly achieve a closed assimilation–retrieval system that could be beneficial for both remote sensing and climate modelling.

Constraining aerosol–cloud interaction in climate models is more challenging. More detailed aerosol schemes have been implemented in many climate models, including explicit consideration of soluble and insoluble species, secondary organic aerosols, the parameterization of aerosol nucleation schemes and CCN activation, for example<sup>204–206</sup>. Cloud microphysics parameterizations have also been refined and ice or mixed-phase cloud schemes have been included<sup>207,208</sup>. Although these improvements can lead to better agreement with observations, they might not lead to improved climate projections, given the large uncertainties in particle microphysical properties and in the processes involved in aerosol–cloud interaction. For example, the increased cloud feedback in the latest climate models, partly related to the updated aerosol–cloud interaction schemes, leads to unrealistically high climate sensitivity<sup>5,209</sup>, highlighting both the complexities and the insufficient understanding of ARI and aerosol–cloud interaction processes, of which the ice–cloud microphysics remains the least understood. The targeted in situ observations discussed here must be implemented and carefully analysed to further clarify the roles of dust, BC and organic aerosols as INPs, upon which ice–cloud microphysical schemes can be improved. As computational resources become yet more abundant, implementing cloud-resolving simulations globally would become possible, which can avoid many parameterizations and provide better constraints on aerosol–cloud interaction and climate sensitivity, though the mechanisms themselves must also be better understood to be modelled accurately.

With a series of planned space and surface observation missions globally, a large increase in the number of observations is anticipated. Combining with systematic characterization of particle microphysical properties, particle ageing and aerosol–cloud interaction processes by in situ measurement, and improved integration of satellite and in situ measurements with modelling, there is hope that the uncertainties in aerosol forcing and climate effects that have persisted for decades will greatly improve in the near future.

#### Data availability

Coupled Model Intercomparison Project Phase 6 (CMIP6) data used in FIGS 1, 3 are from the Earth System Grid Federation, available at <https://esgf-node.llnl.gov/projects/cmip6>. AOD and SSA data used in FIG. 1 are from Aerosol Robotic Network (AERONET), available at <https://aeronet.gsfc.nasa.gov/>.

Published online 24 May 2022

1. Charlson, R. J. et al. Climate forcing by anthropogenic aerosols. *Science* **255**, 423–430 (1992).
2. Prospero, J. et al. The atmospheric aerosol system: An overview. *Rev. Geophys.* **21**, 1607–1629 (1983).
3. Martin, R. V., Jacob, D. J., Yantosca, R. M., Chin, M. & Ginoux, P. Global and regional decreases in tropospheric oxidants from photochemical effects of aerosols. *J. Geophys. Res. Atmos.* **108**, 4097 (2003).
4. IPCC. *Climate Change 2021: The Physical Science Basis* (eds Masson-Delmotte, V. et al.) (Cambridge Univ. Press, 2021).
5. Zelinka, M. D. et al. Causes of higher climate sensitivity in CMIP6 models. *Geophys. Res. Lett.* **47**, e2019GL085782 (2020).
6. Wang, C., Soden, B. J., Yang, W. & Vecchi, G. A. Compensation between cloud feedback and aerosol-cloud interaction in CMIP6 models. *Geophys. Res. Lett.* **48**, e2020GL091024 (2021).
7. Clifß, J. et al. AeroCom phase III multi-model evaluation of the aerosol life cycle and optical properties using ground- and space-based remote sensing as well as surface in situ observations. *Atmos. Chem. Phys.* **21**, 87–128 (2021).
8. Ramaswamy, V. et al. Radiative forcing of climate: the historical evolution of the radiative forcing concept, the forcing agents and their quantification, and applications. *Meteorol. Monogr.* **59**, 14.1–14.101 (2019).
9. Bellouin, N. et al. Bounding global aerosol radiative forcing of climate change. *Rev. Geophys.* **58**, e2019RG000660 (2020).
10. Lee, L. A., Reddington, C. L. & Carslaw, K. S. On the relationship between aerosol model uncertainty and radiative forcing uncertainty. *Proc. Natl Acad. Sci. USA* **113**, 5820–5827 (2016).
11. Loeb, N. G. & Su, W. Direct aerosol radiative forcing uncertainty based on a radiative perturbation analysis. *J. Clim.* **23**, 5288–5293 (2010).
12. Thorsen, T. J., Ferrare, R. A., Kato, S. & Winker, D. M. Aerosol direct radiative effect sensitivity analysis. *J. Clim.* **33**, 6119–6139 (2020).
13. Hansen, J., Sato, M. & Ruedy, R. Radiative forcing and climate response. *J. Geophys. Res. Atmos.* **102**, 6831–6864 (1997).
14. Liao, H. & Seinfeld, J. H. Effect of clouds on direct aerosol radiative forcing of climate. *J. Geophys. Res. Atmos.* **103**, 3781–3788 (1998).
15. Ramanathan, V., Crutzen, P., Kiehl, J. & Rosenfeld, D. Aerosols, climate, and the hydrological cycle. *Science* **294**, 2119–2124 (2001).
16. Kahn, R. A. Reducing the uncertainties in direct aerosol radiative forcing. *Surv. Geophys.* **33**, 701–721 (2012).
17. Kahn, R. A. et al. SAM-CAAM: a concept for acquiring systematic aircraft measurements to characterize aerosol air masses. *Bull. Am. Meteorol. Soc.* **98**, 2215–2228 (2017).
18. Fougnie, B. et al. The multi-viewing multi-channel multi-polarisation imager—Overview of the 3MI polarimetric mission for aerosol and cloud characterization. *J. Quant. Spectrosc. Radiat. Transf.* **219**, 23–32 (2018).
19. Dubovik, O. et al. Polarimetric remote sensing of atmospheric aerosols: Instruments, methodologies, results, and perspectives. *J. Quant. Spectrosc. Radiat. Transf.* **224**, 474–511 (2019).
20. Hasekamp, O. P. et al. Aerosol measurements by SPeXone on the NASA PACE mission: expected retrieval capabilities. *J. Quant. Spectrosc. Radiat. Transf.* **227**, 170–184 (2019).
21. Pérez-Ramírez, D. et al. Optimized profile retrievals of aerosol microphysical properties from simulated spaceborne multiwavelength lidar. *J. Quant. Spectrosc. Radiat. Transf.* **246**, 106932 (2020).
22. Seinfeld, J. H. & Pandis, S. N. *Atmospheric Chemistry and Physics: From Air Pollution to Climate Change* (Wiley, 2016).
23. Dufresne, J.-L., Gautier, C., Ricchiazzi, P. & Fouquart, Y. Longwave scattering effects of mineral aerosols. *J. Atmos. Sci.* **59**, 1959–1966 (2002).
24. Chand, D., Wood, R., Anderson, T., Satheesh, S. & Charlson, R. Satellite-derived direct radiative effect of aerosols dependent on cloud cover. *Nat. Geosci.* **2**, 181–184 (2009).
25. Mishra, A. K., Koren, I. & Rudich, Y. Effect of aerosol vertical distribution on aerosol-radiation interaction: A theoretical prospect. *Heliyon* **1**, e00036 (2015).
26. Dubovik, O. et al. Variability of absorption and optical properties of key aerosol types observed in worldwide locations. *J. Atmos. Sci.* **59**, 590–608 (2002).
27. Mishchenko, M. I., Hovenier, J. W. & Travis, L. D. (eds) *Light Scattering by Nonspherical Particles: Theory, Measurements, and Applications* (Academic Press, 2000).
28. Nousiainen, T., Zubko, E., Lindqvist, H., Kahnert, M. & Tynnelä, J. Comparison of scattering by different nonspherical, wavelength-scale particles. *J. Quant. Spectrosc. Radiat. Transf.* **113**, 2391–2405 (2012).
29. Mishchenko, M. I. & Travis, L. D. Satellite retrieval of aerosol properties over the ocean using polarization as well as intensity of reflected sunlight. *J. Geophys. Res. Atmos.* **102**, 16989–17013 (1997).
30. Mylonaki, M. et al. Aerosol type classification analysis using EARLINET multiwavelength and depolarization lidar observations. *Atmos. Chem. Phys.* **21**, 2211–2227 (2021).
31. Mishchenko, M. I. et al. Monitoring of aerosol forcing of climate from space: analysis of measurement requirements. *J. Quant. Spectrosc. Radiat. Transf.* **88**, 149–161 (2004).
32. Bond, T. C. & Bergstrom, R. W. Light absorption by carbonaceous particles: An investigative review. *Aerosol Sci. Technol.* **40**, 27–67 (2006).
33. Bergstrom, R. W. et al. Spectral absorption properties of atmospheric aerosols. *Atmos. Chem. Phys.* **7**, 5937–5943 (2007).
34. Samsel, B. H. et al. Aerosol absorption: Progress towards global and regional constraints. *Curr. Clim. Change Rep.* **4**, 65–83 (2018).
35. Satheesh, S. & Ramanathan, V. Large differences in tropospheric aerosol forcing at the top of the atmosphere and Earth's surface. *Nature* **405**, 60–63 (2000).
36. Ramanathan, V. & Carmichael, G. Global and regional climate changes due to black carbon. *Nat. Geosci.* **1**, 221–227 (2008).
37. Ding, A. et al. Enhanced haze pollution by black carbon in megacities in China. *Geophys. Res. Lett.* **43**, 2873–2879 (2016).
38. Pendergrass, A. & Hartmann, D. Global-mean precipitation and black carbon in AR4 simulations. *Geophys. Res. Lett.* **39**, L01703 (2012).
39. Takemura, T., Nakajima, T., Dubovik, O., Holben, B. N. & Kinne, S. Single-scattering albedo and radiative forcing of various aerosol species with a global three-dimensional model. *J. Clim.* **15**, 333–352 (2002).
40. Wilcox, E. Direct and semi-direct radiative forcing of smoke aerosols over clouds. *Atmos. Chem. Phys.* **12**, 139–149 (2012).
41. Myhre, G. et al. Cloudy-sky contributions to the direct aerosol effect. *Atmos. Chem. Phys.* **20**, 8855–8865 (2020).
42. Samsel, B. H. et al. Black carbon vertical profiles strongly affect its radiative forcing uncertainty. *Atmos. Chem. Phys.* **13**, 2423–2434 (2013).
43. Haywood, J. & Ramaswamy, V. Global sensitivity studies of the direct radiative forcing due to anthropogenic sulfate and black carbon aerosols. *J. Geophys. Res. Atmos.* **103**, 6043–6058 (1998).
44. Chylek, P., Ramaswamy, V. & Srivastava, V. Albedo of soot-contaminated snow. *J. Geophys. Res. Oceans* **88**, 10837–10843 (1983).
45. Hansen, J. & Nazarenko, L. Soot climate forcing via snow and ice albedos. *Proc. Natl Acad. Sci. USA* **101**, 423–428 (2004).
46. Doherty, S., Warren, S., Grenfell, T., Clarke, A. & Brandt, R. Light-absorbing impurities in Arctic snow. *Atmos. Chem. Phys.* **10**, 11647–11680 (2010).
47. Sarangi, C. et al. Dust dominates high-altitude snow darkening and melt over high-mountain Asia. *Nat. Clim. Change* **10**, 1045–1051 (2020).
48. Ramana, M. et al. Warming influenced by the ratio of black carbon to sulphate and the black-carbon source. *Nat. Geosci.* **3**, 542–545 (2010).
49. Jacobson, M. Z. Global direct radiative forcing due to multicomponent anthropogenic and natural aerosols. *J. Geophys. Res. Atmos.* **106**, 1551–1568 (2001).
50. Chylek, P. & Coakley, J. A. Aerosols and climate. *Science* **183**, 75–77 (1974).
51. Ackerman, T. P. & Toon, O. B. Absorption of visible radiation in atmosphere containing mixtures of absorbing and nonabsorbing particles. *Appl. Opt.* **20**, 3661–3668 (1981).
52. Chylek, P., Ramaswamy, V. & Cheng, R. J. Effect of graphitic carbon on the albedo of clouds. *J. Atmos. Sci.* **41**, 3076–3084 (1984).
53. Jacobson, M. Z. Strong radiative heating due to the mixing state of black carbon in atmospheric aerosols. *Nature* **409**, 695–697 (2001).
54. Cappa, C. D. et al. Radiative absorption enhancements due to the mixing state of atmospheric black carbon. *Science* **337**, 1078–1081 (2012).
55. Vuolo, M. R., Schulz, M., Balkanski, Y. & Takemura, T. A new method for evaluating the impact of vertical distribution on aerosol radiative forcing in general circulation models. *Atmos. Chem. Phys.* **14**, 877–897 (2014).
56. Lohmann, U. & Feichter, J. Global indirect aerosol effects: a review. *Atmos. Chem. Phys.* **5**, 715–737 (2005).
57. Twomey, S. The influence of pollution on the shortwave albedo of clouds. *J. Atmos. Sci.* **34**, 1149–1152 (1977).
58. Han, Q., Rossow, W. B., Zeng, J. & Welch, R. Three different behaviors of liquid water path of water clouds in aerosol–cloud interactions. *J. Atmos. Sci.* **59**, 726–735 (2002).
59. Ackerman, A. S., Kirkpatrick, M. P., Stevens, D. E. & Toon, O. B. The impact of humidity above stratiform clouds on indirect aerosol climate forcing. *Nature* **432**, 1014–1017 (2004).
60. Chen, Y.-C., Christensen, M. W., Stephens, G. L. & Seinfeld, J. H. Satellite-based estimate of global aerosol–cloud radiative forcing by marine warm clouds. *Nat. Geosci.* **7**, 643–646 (2014).
61. Grysperdt, E., Stier, P. & Partridge, D. Satellite observations of cloud regime development: the role of aerosol processes. *Atmos. Chem. Phys.* **14**, 1141–1158 (2014).
62. Sato, Y. et al. Aerosol effects on cloud water amounts were successfully simulated by a global cloud-system resolving model. *Nat. Commun.* **9**, 985 (2018).
63. Toll, V., Christensen, M., Quaas, J. & Bellouin, N. Weak average liquid-cloud-water response to anthropogenic aerosols. *Nature* **572**, 51–55 (2019).
64. Penner, J. E., Zhou, C., Garnier, A. & Mitchell, D. L. Anthropogenic aerosol indirect effects in cirrus clouds. *J. Geophys. Res. Atmos.* **123**, 11,652–11,677 (2018).
65. McGraw, Z., Storelvmo, T., Samsel, B. H. & Stjern, C. W. Global radiative impacts of black carbon acting as ice nucleating particles. *Geophys. Res. Lett.* **47**, e2020GL089056 (2020).
66. Adams, M. P. et al. A major combustion aerosol event had a negligible impact on the atmospheric ice-nucleating particle population. *J. Geophys. Res. Atmos.* **125**, e2020JD032938 (2020).
67. Stjern, C. W. et al. Rapid adjustments cause weak surface temperature response to increased black carbon concentrations. *J. Geophys. Res. Atmos.* **122**, 11,462–11,481 (2017).
68. Smith, C. et al. Understanding rapid adjustments to diverse forcing agents. *Geophys. Res. Lett.* **45**, 12,023–12,031 (2018).
69. Thornhill, G. D. et al. Effective radiative forcing from emissions of reactive gases and aerosols—a multi-model comparison. *Atmos. Chem. Phys.* **21**, 853–874 (2021).
70. Conant, W. C., Nenes, A. & Seinfeld, J. H. Black carbon radiative heating effects on cloud microphysics and implications for the aerosol indirect effect 1. Extended Köhler theory. *J. Geophys. Res. Atmos.* **107**, AAC 23-1–AAC 23-9 (2002).
71. Holben, B. N. et al. AERONET — A federated instrument network and data archive for aerosol characterization. *Remote Sens. Environ.* **66**, 1–16 (1998).
72. Levy, R. et al. The Collection 6 MODIS aerosol products over land and ocean. *Atmos. Meas. Tech.* **6**, 2989–3034 (2013).
73. Omar, A. H. et al. The CALIPSO automated aerosol classification and lidar ratio selection algorithm. *J. Atmos. Ocean. Technol.* **26**, 1994–2014 (2009).
74. Kahn, R. A. & Gattley, B. J. An analysis of global aerosol type as retrieved by MISR. *J. Geophys. Res. Atmos.* **120**, 4248–4281 (2015).
75. Herich, H. et al. In situ determination of atmospheric aerosol composition as a function of hygroscopic growth. *J. Geophys. Res. Atmos.* **113**, D16213 (2008).
76. Moffet, R. C. & Prather, K. A. In-situ measurements of the mixing state and optical properties of soot with implications for radiative forcing estimates. *Proc. Natl Acad. Sci. USA* **106**, 11872–11877 (2009).
77. Laj, P. et al. A global analysis of climate-relevant aerosol properties retrieved from the network of Global Atmosphere Watch (GAW) near-surface observatories. *Atmos. Meas. Tech.* **13**, 4353–4392 (2020).
78. Ziemba, L. D. et al. Airborne observations of aerosol extinction by in situ and remote-sensing techniques: Evaluation of particle hygroscopicity. *Geophys. Res. Lett.* **40**, 417–422 (2013).
79. Nakajima, T. & Tanaka, M. Algorithms for radiative intensity calculations in moderately thick atmospheres using a truncation approximation. *J. Quant. Spectrosc. Radiat. Transf.* **40**, 51–69 (1988).

80. Dubovik, O. & King, M. D. A flexible inversion algorithm for retrieval of aerosol optical properties from Sun and sky radiance measurements. *J. Geophys. Res. Atmos.* **105**, 20673–20696 (2000).
81. Sinyuk, A. et al. The AERONET Version 3 aerosol retrieval algorithm, associated uncertainties and comparisons to Version 2. *Atmos. Meas. Tech.* **13**, 3375–3411 (2020).
82. Dubovik, O. et al. Accuracy assessments of aerosol optical properties retrieved from Aerosol Robotic Network (AERONET) Sun and sky radiance measurements. *J. Geophys. Res. Atmos.* **105**, 9791–9806 (2000).
83. Takamura, T. Overview of SKYNET and its activities. *Opt. Pura Apl.* **37**, 3303–3308 (2004).
84. Che, H. et al. Ground-based aerosol climatology of China: aerosol optical depths from the China Aerosol Remote Sensing Network (CARSONET) 2002–2013. *Atmos. Chem. Phys.* **15**, 7619–7652 (2015).
85. Singh, A. et al. An overview of airborne measurement in Nepal—Part 1: Vertical profile of aerosol size, number, spectral absorption, and meteorology. *Atmos. Chem. Phys.* **19**, 245–258 (2019).
86. Li, C., Li, J., Dubovik, O., Zeng, Z.-C. & Yung, Y. L. Impact of aerosol vertical distribution on aerosol optical depth retrieval from passive satellite sensors. *Remote Sens.* **12**, 1524 (2020).
87. Klett, J. D. Lidar inversion with variable backscatter/extinction ratios. *Appl. Opt.* **24**, 1638–1643 (1985).
88. Burton, S. P. et al. Information content and sensitivity of the  $3\beta + 2\alpha$  lidar measurement system for aerosol microphysical retrievals. *Atmos. Meas. Tech.* **9**, 5555–5574 (2016).
89. Welton, E. J., Campbell, J. R., Spinhrne, J. D. & Scott III, V. S. in *Lidar Remote Sensing for Industry and Environment Monitoring* 151–158 (International Society for Optics and Photonics, 2001).
90. Bösenberg, J. et al. EARLINET: a European aerosol research lidar network. *Adv. Laser Remote Sensing* **155**, 6–181 (2001).
91. Antuña-Marrero, J. C. et al. LALINET: The first Latin American-born regional atmospheric observational network. *Bull. Am. Meteorol. Soc.* **98**, 1255–1275 (2017).
92. Lopatin, A. et al. Synergy processing of diverse ground-based remote sensing and in situ data using the GRASP algorithm: applications to radiometer, lidar and radiosonde observations. *Atmos. Meas. Tech.* **14**, 2575–2614 (2021).
93. Kaufman, Y. et al. Passive remote sensing of tropospheric aerosol and atmospheric correction for the aerosol effect. *J. Geophys. Res. Atmos.* **102**, 16815–16830 (1997).
94. Torres, O., Bhartia, P., Herman, J., Ahmad, Z. & Gleason, J. Derivation of aerosol properties from satellite measurements of backscattered ultraviolet radiation: Theoretical basis. *J. Geophys. Res. Atmos.* **103**, 17099–17110 (1998).
95. Hammer, M. S. et al. Interpreting the ultraviolet aerosol index observed with the OMI satellite instrument to understand absorption by organic aerosols: implications for atmospheric oxidation and direct radiative effects. *Atmos. Chem. Phys.* **16**, 2507–2523 (2016).
96. Mahowald, N. M. & Dufresne, J. L. Sensitivity of TOMS aerosol index to boundary layer height: Implications for detection of mineral aerosol sources. *Geophys. Res. Lett.* **31**, L03103 (2004).
97. Torres, O. et al. Aerosols and surface UV products from Ozone Monitoring Instrument observations: An overview. *J. Geophys. Res. Atmos.* **112**, D24S47 (2007).
98. Martonchik, J. V., Kahn, R. A. & Diner, D. J. in *Satellite Aerosol Remote Sensing Over Land* 267–293 (Springer, 2009).
99. Hasekamp, O. P. & Landgraf, J. Retrieval of aerosol properties over the ocean from multispectral single-viewing-angle measurements of intensity and polarization: Retrieval approach, information content, and sensitivity study. *J. Geophys. Res. Atmos.* **110**, D20207 (2005).
100. Dubovik, O. et al. Statistically optimized inversion algorithm for enhanced retrieval of aerosol properties from spectral multi-angle polarimetric satellite observations. *Atmos. Meas. Tech.* **4**, 975–1018 (2011).
101. Schutgens, N. et al. AEROCOM and AEROSAT AAOD and SSA study—Part 1: Evaluation and intercomparison of satellite measurements. *Atmos. Chem. Phys.* **21**, 6895–6917 (2021).
102. Chen, C. et al. Validation of GRASP algorithm product from POLDER/PARASOL data and assessment of multi-angular polarimetry potential for aerosol monitoring. *Earth Syst. Sci. Data* **12**, 3573–3620 (2020).
103. Xu, F. et al. Coupled retrieval of aerosol properties and land surface reflection using the Airborne Multiangle SpectroPolarimetric Imager. *J. Geophys. Res. Atmos.* **122**, 7004–7026 (2017).
104. Torres, O., Jethva, H. & Bhartia, P. Retrieval of aerosol optical depth above clouds from OMI observations: Sensitivity analysis and case studies. *J. Atmos. Sci.* **69**, 1037–1053 (2012).
105. Ahn, C., Torres, O., Jethva, H., Tiruchirappalli, R. & Huang, L. K. Evaluation of aerosol properties observed by DSCOVR/EPIC instrument from the Earth-Sun Lagrange 1 orbit. *J. Geophys. Res. Atmos.* **126**, e2020JD033651 (2021).
106. Wu, L. et al. Passive remote sensing of aerosol layer height using near-UV multiangle polarization measurements. *Geophys. Res. Lett.* **43**, 8783–8790 (2016).
107. Zeng, Z.-C. et al. Constraining aerosol vertical profile in the boundary layer using hyperspectral measurements of oxygen absorption. *Geophys. Res. Lett.* **45**, 10,772–10,780 (2018).
108. Zeng, Z.-C. et al. Constraining the vertical distribution of coastal dust aerosol using OCO-2 O<sub>2</sub> A-band measurements. *Remote Sens. Environ.* **236**, 111494 (2020).
109. Xu, X. et al. Detecting layer height of smoke aerosols over vegetated land and water surfaces via oxygen absorption bands: hourly results from EPIC/DSCOVR in deep space. *Atmos. Meas. Tech.* **12**, 3269–3288 (2019).
110. Nelson, D. L., Garay, M. J., Kahn, R. A. & Dunst, B. A. Stereoscopic height and wind retrievals for aerosol plumes with the MISR Interactive Explorer (MINX). *Remote Sens.* **5**, 4593–4628 (2013).
111. McGill, M. J., Yorks, J. E., Scott, V. S., Kupchok, A. W. & Selmer, P. A. in *Lidar Remote Sensing for Environmental Monitoring XV* (International Society for Optics and Photonics, 2016).
112. Noel, V., Chepfer, H., Chiriaco, M. & Yorks, J. The diurnal cycle of cloud profiles over land and ocean between 51°S and 51°N, seen by the CATS spaceborne lidar from the International Space Station. *Atmos. Chem. Phys.* **18**, 9457–9473 (2018).
113. Thorsen, T. J., Winker, D. M. & Ferrare, R. A. Uncertainty in observational estimates of the aerosol direct radiative effect and forcing. *J. Clim.* **34**, 195–214 (2021).
114. Rosenfeld, D., Sherwood, S., Wood, R. & Donner, L. Climate effects of aerosol-cloud interactions. *Science* **343**, 379–380 (2014).
115. Gryspeerdt, E. et al. Constraining the instantaneous aerosol influence on cloud albedo. *Proc. Natl Acad. Sci. USA* **114**, 4899–4904 (2017).
116. Heintzenberg, J. et al. Intercomparisons and aerosol calibrations of 12 commercial integrating nephelometers of three manufacturers. *J. Atmos. Oceanic Technol.* **23**, 902–914 (2006).
117. Eleftheriadis, K., Vratolis, S. & Nyeki, S. Aerosol black carbon in the European Arctic: measurements at Zeppelin station, Ny-Ålesund, Svalbard from 1998–2007. *Geophys. Res. Lett.* **36**, L02809 (2009).
118. Bond, T. C., Anderson, T. L. & Campbell, D. Calibration and intercomparison of filter-based measurements of visible light absorption by aerosols. *Aerosol Sci. Technol.* **30**, 582–600 (1999).
119. Seinfeld, J. H. et al. Improving our fundamental understanding of the role of aerosol–cloud interactions in the climate system. *Proc. Natl Acad. Sci. USA* **113**, 5781–5790 (2016).
120. van der Werf, G. R. et al. Interannual variability in global biomass burning emissions from 1997 to 2004. *Atmos. Chem. Phys.* **6**, 3423–3441 (2006).
121. Hsu, N. et al. Global and regional trends of aerosol optical depth over land and ocean using SeaWiFS measurements from 1997 to 2010. *Atmos. Chem. Phys.* **12**, 8037–8053 (2012).
122. Zhang, J. & Reid, J. A decadal regional and global trend analysis of the aerosol optical depth using a data-assimilation grade over-water MODIS and Level 2 MISR aerosol products. *Atmos. Chem. Phys.* **10**, 10949–10963 (2010).
123. Liu, M. & Matsui, H. Aerosol radiative forcings induced by substantial changes in anthropogenic emissions in China from 2008 to 2016. *Atmos. Chem. Phys.* **21**, 5965–5982 (2021).
124. Li, J., Carlson, B. E., Dubovik, O. & Laci, A. A. Recent trends in aerosol optical properties derived from AERONET measurements. *Atmos. Chem. Phys.* **14**, 12271–12289 (2014).
125. Lyapustin, A. et al. Reduction of aerosol absorption in Beijing since 2007 from MODIS and AERONET. *Geophys. Res. Lett.* **38**, L10803 (2011).
126. Mishchenko, M. I. et al. Aerosol retrievals from channel-1 and -2 AVHRR radiances: Long-term trends updated and revisited. *J. Quant. Spectrosc. Radiat. Transf.* **113**, 1974–1980 (2012).
127. Diffenbaugh, N. S. et al. The COVID-19 lockdowns: a window into the Earth System. *Nat. Rev. Earth Environ.* **1**, 470–481 (2020).
128. Gettelman, A., Lamboll, R., Bardeen, C., Forster, P. & Watson-Parris, D. Climate impacts of COVID-19 induced emission changes. *Geophys. Res. Lett.* **48**, e2020GL091805 (2021).
129. Reifenberg, S. F. et al. Impact of reduced emissions on direct and indirect aerosol radiative forcing during COVID-19 lockdown in Europe. *Atmos. Chem. Phys. Discuss.* <https://doi.org/10.5194/acp-2021-1005> (2021).
130. Ming, Y. et al. Assessing the influence of COVID-19 on the shortwave radiative fluxes over the East Asian marginal seas. *Geophys. Res. Lett.* **48**, e2020GL091699 (2021).
131. Bowman, D. M. et al. Vegetation fires in the Anthropocene. *Nat. Rev. Earth Environ.* **1**, 500–515 (2020).
132. Evangelou, N. et al. Changes in black carbon emissions over Europe due to COVID-19 lockdowns. *Atmos. Chem. Phys.* **21**, 2675–2692 (2021).
133. Huang, X. et al. Enhanced secondary pollution offset reduction of primary emissions during COVID-19 lockdown in China. *Natl Sci. Rev.* **8**, nwa137 (2021).
134. Weber, J. et al. Minimal climate impacts from short-lived climate forcers following emission reductions related to the COVID-19 pandemic. *Geophys. Res. Lett.* **47**, e2020GL090326 (2020).
135. Forster, P. M. et al. Current and future global climate impacts resulting from COVID-19. *Nat. Clim. Change* **10**, 913–919 (2020).
136. Li, J. Pollution trends in China from 2000 to 2017: A multi-sensor view from space. *Remote Sens.* **12**, 208 (2020).
137. Turnock, S. T. et al. Historical and future changes in air pollutants from CMIP6 models. *Atmos. Chem. Phys.* **20**, 14547–14579 (2020).
138. Paasonen, P. et al. Warming-induced increase in aerosol number concentration likely to moderate climate change. *Nat. Geosci.* **6**, 438–442 (2013).
139. Touma, D., Stevenson, S., Lehner, F. & Coats, S. Human-driven greenhouse gas and aerosol emissions cause distinct regional impacts on extreme fire weather. *Nat. Commun.* **12**, 212 (2021).
140. Allen, R. J., Landuyt, W. & Rumbold, S. T. An increase in aerosol burden and radiative effects in a warmer world. *Nat. Clim. Change* **6**, 269–274 (2016).
141. Mahowald, N. M., Lamarque, J. F., Tie, X. X. & Wolf, E. Sea-salt aerosol response to climate change: Last Glacial Maximum, preindustrial, and doubled carbon dioxide climates. *J. Geophys. Res. Atmos.* **111**, D05303 (2006).
142. Struthers, H. et al. Climate-induced changes in sea salt aerosol number emissions: 1870 to 2100. *J. Geophys. Res. Atmos.* **118**, 670–682 (2013).
143. Liao, H., Chen, W. T. & Seinfeld, J. H. Role of climate change in global predictions of future tropospheric ozone and aerosols. *J. Geophys. Res. Atmos.* **111**, D12304 (2006).
144. Jones, A., Haywood, J. M. & Boucher, O. Aerosol forcing, climate response and climate sensitivity in the Hadley Centre climate model. *J. Geophys. Res. Atmos.* **112**, D20211 (2007).
145. Gidden, M. J. et al. Global emissions pathways under different socioeconomic scenarios for use in CMIP6: a dataset of harmonized emissions trajectories through the end of the century. *Geosci. Model Dev.* **12**, 1443–1475 (2019).
146. Kok, J. F., Ward, D. S., Mahowald, N. M. & Evan, A. T. Global and regional importance of the direct dust-climate feedback. *Nat. Commun.* **9**, 241 (2018).
147. Levy, H. et al. The roles of aerosol direct and indirect effects in past and future climate change. *J. Geophys. Res. Atmos.* **118**, 4521–4532 (2013).
148. Ramaswamy, V., Ming, Y. & Schwarzkopf, M. D. in *Hydrological Aspects of Climate Change* (eds Pandey, A., Kumar, S. & Kumar, A.) 61–76 (Springer, 2021).
149. Meehl, G. A., Boer, G. J., Covey, C., Latif, M. & Stouffer, R. J. The coupled model intercomparison project (CMIP). *Bull. Am. Meteorol. Soc.* **81**, 313–318 (2000).



150. Schulz, M. et al. Radiative forcing by aerosols as derived from the AeroCom present-day and pre-industrial simulations. *Atmos. Chem. Phys.* **6**, 5225–5246 (2006).
151. Shindell, D. T. et al. Radiative forcing in the ACCMIP historical and future climate simulations. *Atmos. Chem. Phys.* **13**, 2939–2974 (2013).
152. Yu, H. et al. A review of measurement-based assessments of the aerosol direct radiative effect and forcing. *Atmos. Chem. Phys.* **6**, 613–666 (2006).
153. Quaas, J., Boucher, O., Bellouin, N. & Kinne, S. Satellite-based estimate of the direct and indirect aerosol climate forcing. *J. Geophys. Res. Atmos.* **113**, D05204 (2008).
154. Hasekamp, O. P., Gryspeerdt, E. & Quaas, J. Analysis of polarimetric satellite measurements suggests stronger cooling due to aerosol-cloud interactions. *Nat. Commun.* **10**, 5405 (2019).
155. Gryspeerdt, E. et al. Surprising similarities in model and observational aerosol radiative forcing estimates. *Atmos. Chem. Phys.* **20**, 613–623 (2020).
156. Allen, R. J. & Landuyt, W. The vertical distribution of black carbon in CMIP5 models: Comparison to observations and the importance of convective transport. *J. Geophys. Res. Atmos.* **119**, 4808–4835 (2014).
157. Regayre, L. A. et al. The value of remote marine aerosol measurements for constraining radiative forcing uncertainty. *Atmos. Chem. Phys.* **20**, 10063–10072 (2020).
158. Carslaw, K. et al. Large contribution of natural aerosols to uncertainty in indirect forcing. *Nature* **503**, 67–71 (2013).
159. Penner, J. E., Zhou, C. & Xu, L. Consistent estimates from satellites and models for the first aerosol indirect forcing. *Geophys. Res. Lett.* **39**, L13810 (2012).
160. Carslaw, K. S. et al. Aerosols in the pre-industrial atmosphere. *Curr. Clim. Change Rep.* **3**, 1–15 (2017).
161. Ocko, I. B., Ramaswamy, V., Ginoux, P., Ming, Y. & Horowitz, L. W. Sensitivity of scattering and absorbing aerosol direct radiative forcing to physical climate factors. *J. Geophys. Res. Atmos.* **117**, D20203 (2012).
162. Myhre, G. & Samset, B. H. Standard climate models radiation codes underestimate black carbon radiative forcing. *Atmos. Chem. Phys.* **15**, 2883–2888 (2015).
163. Ramaswamy, V. & Chen, C. T. Linear additivity of climate response for combined albedo and greenhouse perturbations. *Geophys. Res. Lett.* **24**, 567–570 (1997).
164. Rotstayn, L. D. & Lohmann, U. Tropical rainfall trends and the indirect aerosol effect. *J. Clim.* **15**, 2103–2116 (2002).
165. Ming, Y. & Ramaswamy, V. Nonlinear climate and hydrological responses to aerosol effects. *J. Clim.* **22**, 1329–1339 (2009).
166. Xie, S.-P., Lu, B. & Xiang, B. Similar spatial patterns of climate responses to aerosol and greenhouse gas changes. *Nat. Geosci.* **6**, 828–832 (2013).
167. Smith, D. M. et al. Role of volcanic and anthropogenic aerosols in the recent global surface warming slowdown. *Nat. Clim. Change* **6**, 936–940 (2016).
168. Menary, M. B. et al. Aerosol-forced AMOC changes in CMIP6 historical simulations. *Geophys. Res. Lett.* **47**, e2020GL088166 (2020).
169. Ramanathan, V. et al. Atmospheric brown clouds: Impacts on South Asian climate and hydrological cycle. *Proc. Natl Acad. Sci. USA* **102**, 5326–5333 (2005).
170. Chung, C. E. & Ramanathan, V. Weakening of North Indian SST gradients and the monsoon rainfall in India and the Sahel. *J. Clim.* **19**, 2036–2045 (2006).
171. Bollasina, M. A., Ming, Y. & Ramaswamy, V. Anthropogenic aerosols and the weakening of the South Asian summer monsoon. *Science* **334**, 502–505 (2011).
172. Navarro, J. A. et al. Amplification of Arctic warming by past air pollution reductions in Europe. *Nat. Geosci.* **9**, 277–281 (2016).
173. Wang, Y. et al. Reduced European aerosol emissions suppress winter extremes over northern Eurasia. *Nat. Clim. Change* **10**, 225–230 (2020).
174. Polson, D., Bollasina, M., Hegerl, G. C. & Wilcox, L. Decreased monsoon precipitation in the Northern Hemisphere due to anthropogenic aerosols. *Geophys. Res. Lett.* **41**, 6023–6029 (2014).
175. Chung, E.-S. & Soden, B. J. Hemispheric climate shifts driven by anthropogenic aerosol–cloud interactions. *Nat. Geosci.* **10**, 566–571 (2017).
176. Xu, Y. & Xie, S.-P. Ocean mediation of tropospheric response to reflecting and absorbing aerosols. *Atmos. Chem. Phys.* **15**, 5827–5833 (2015).
177. Suzuki, K. & Takemura, T. Perturbations to global energy budget due to absorbing and scattering aerosols. *J. Geophys. Res. Atmos.* **124**, 2194–2209 (2019).
178. Ocko, I. B., Ramaswamy, V. & Ming, Y. Contrasting climate responses to the scattering and absorbing features of anthropogenic aerosol forcings. *J. Clim.* **27**, 5329–5345 (2014).
179. Kim, M. J., Yeh, S. W. & Park, R. J. Effects of sulfate aerosol forcing on East Asian summer monsoon for 1985–2010. *Geophys. Res. Lett.* **43**, 1364–1372 (2016).
180. Jiang, Y. et al. Anthropogenic aerosol effects on East Asian winter monsoon: The role of black carbon-induced Tibetan Plateau warming. *J. Geophys. Res. Atmos.* **122**, 5883–5902 (2017).
181. Liu, Z. et al. A model investigation of aerosol-induced changes in the East Asian winter monsoon. *Geophys. Res. Lett.* **46**, 10186–10195 (2019).
182. Menon, S., Hansen, J., Nazarenko, L. & Luo, Y. Climate effects of black carbon aerosols in China and India. *Science* **297**, 2250–2253 (2002).
183. Zhang, Y. et al. Impact of biomass burning aerosol on the monsoon circulation transition over Amazonia. *Geophys. Res. Lett.* **36**, L10814 (2009).
184. Undorf, S. et al. Detectable impact of local and remote anthropogenic aerosols on the 20th century changes of West African and South Asian monsoon precipitation. *J. Geophys. Res. Atmos.* **123**, 4871–4889 (2018).
185. Bollasina, M. A., Ming, Y., Ramaswamy, V., Schwarzkopf, M. D. & Naik, V. Contribution of local and remote anthropogenic aerosols to the twentieth century weakening of the South Asian Monsoon. *Geophys. Res. Lett.* **41**, 680–687 (2014).
186. Qiu, Y., Liao, H., Zhang, R. & Hu, J. Simulated impacts of direct radiative effects of scattering and absorbing aerosols on surface layer aerosol concentrations in China during a heavily polluted event in February 2014. *J. Geophys. Res. Atmos.* **122**, 5955–5975 (2017).
187. Li, Z. et al. Aerosol and boundary-layer interactions and impact on air quality. *Nat. Sci. Rev.* **4**, 810–833 (2017).
188. Thornhill, G. et al. Climate-driven chemistry and aerosol feedbacks in CMIP6 Earth system models. *Atmos. Chem. Phys.* **21**, 1105–1126 (2021).
189. Mishchenko, M. I. et al. Accurate monitoring of terrestrial aerosols and total solar irradiance: introducing the Glory mission. *Bull. Am. Meteorol. Soc.* **88**, 677–692 (2007).
190. Martins, J. V., Fernandez-Borda, R., McBride, B., Remer, L. & Barbosa, H. M. in *IGARSS/IEEE International Geoscience and Remote Sensing Symposium* 6304–6307 (IEEE, 2018).
191. Pérez-Ramírez, D. et al. Retrievals of aerosol single scattering albedo by multiwavelength lidar measurements: Evaluations with NASA Langley HSRL-2 during discover-AQ field campaigns. *Remote Sens. Environ.* **222**, 144–164 (2019).
192. Starr, D. in *Hyperspectral Imaging and Sounding of the Environment* (Optical Society of America, 2011).
193. Gorman, E. T. et al. in *Sensors, Systems, and Next-Generation Satellites XXIII* (International Society for Optics and Photonics, 2019).
194. Braun, S. A. et al. *The NASA Decadal Survey Observing-System Study for Aerosols and Clouds, Convection, and Precipitation (ACCP)* (NASA, 2020).
195. Illingworth, A. J. et al. The EarthCARE satellite: The next step forward in global measurements of clouds, aerosols, precipitation, and radiation. *Bull. Am. Meteorol. Soc.* **96**, 1311–1332 (2015).
196. Hansen, J., Rossow, W. B. & Fung, I. *Long-Term Monitoring of Global Climate Forcings and Feedbacks* Vol. 3234 (NASA, 1993).
197. Bocquet, M. et al. Data assimilation in atmospheric chemistry models: current status and future prospects for coupled chemistry meteorology models. *Atmos. Chem. Phys.* **15**, 5325–5358 (2015).
198. Chen, C. et al. Retrieval of desert dust and carbonaceous aerosol emissions over Africa from POLDER/PARASOL products generated by the GRASP algorithm. *Atmos. Chem. Phys.* **18**, 12551–12580 (2018).
199. Tsikerdekis, A., Schutgens, N. A. & Hasekamp, O. P. Assimilating aerosol optical properties related to size and absorption from POLDER/PARASOL with an ensemble data assimilation system. *Atmos. Chem. Phys.* **21**, 2637–2674 (2021).
200. El Amraoui, L. et al. Aerosol data assimilation in the MOCAGE chemical transport model during the TRAQA/ChArMEX campaign: lidar observations. *Atmos. Meas. Tech.* **13**, 4645–4667 (2020).
201. Liang, Y. et al. Development of a three-dimensional variational assimilation system for lidar profile data based on a size-resolved aerosol model in WRF–Chem model v3.9.1 and its application in PM<sub>2.5</sub> forecasts across China. *Geosci. Model Dev.* **13**, 6285–6301 (2020).
202. Randles, C. et al. The MERRA-2 aerosol reanalysis, 1980 onward. Part I: System description and data assimilation evaluation. *J. Clim.* **30**, 6823–6850 (2017).
203. Yumimoto, K., Tanaka, T. Y., Oshima, N. & Maki, T. JRAero: the Japanese reanalysis for aerosol v1.0. *Geosci. Model Dev.* **10**, 3225–3253 (2017).
204. Zhu, J. & Penner, J. E. Global modeling of secondary organic aerosol with organic nucleation. *J. Geophys. Res. Atmos.* **124**, 8260–8286 (2019).
205. Horowitz, L. W. et al. The GFDL global atmospheric chemistry-climate model AM4.1: Model description and simulation characteristics. *J. Adv. Model. Earth Syst.* **12**, e2019MS002032 (2020).
206. Chang, D. et al. Aerosol physicochemical effects on CCN activation simulated with the chemistry-climate model EMAC. *Atmos. Environ.* **162**, 127–140 (2017).
207. Eidhammer, T., Morrison, H., Mitchell, D., Gettelman, A. & Erfani, E. Improvements in global climate model microphysics using a consistent representation of ice particle properties. *J. Clim.* **30**, 609–629 (2017).
208. Righi, M. et al. Coupling aerosols to (cirrus) clouds in the global EMAC-MADE3 aerosol–climate model. *Geosci. Model Dev.* **13**, 1635–1661 (2020).
209. Meehl, G. A. et al. Context for interpreting equilibrium climate sensitivity and transient climate response from the CMIP6 Earth system models. *Sci. Adv.* **6**, eaba1981 (2020).
210. Zhang, L. et al. Clear-sky direct aerosol radiative forcing uncertainty associated with aerosol optical properties based on CMIP6 models. *J. Clim.* **35**, 3007–3019 (2022).

#### Acknowledgements

J.L., L.Z. and Y.D. acknowledge funding from National Natural Science Foundation of China grant nos. 41975023 and 42175144. O.D. appreciates support from the Chemical and Physical Properties of the Atmosphere Project funded by the French National Research Agency through the Programme d'Investissement d'Avenir under contract ANR-11-LABX-0005-01, the Regional Council "Hauts-de-France", and the European Funds for Regional Economic Development.

#### Author contributions

J.L., B.E.C., A.A.L. and Y.L.Y. led the Review. J.L. wrote the initial draft and prepared Fig. 2, Box 1 and Supplementary Fig. 1. L.Z. prepared Fig. 1, Fig. 4 and Supplementary Figs 2, 3. Y.D. prepared Fig. 3 and Table 1. All authors contributed to the manuscript preparation, interpretation, discussion and writing.

#### Competing interests

The authors declare no competing interests.

#### Peer review information

*Nature Reviews Earth & Environment* thanks Fangqun Yu, Otto Hasekamp and the other, anonymous, reviewer(s) for their contribution to the peer review of this work.

#### Publisher's note

Springer Nature remains neutral with regard to jurisdictional claims in published maps and institutional affiliations.

#### Supplementary information

The online version contains supplementary material available at <https://doi.org/10.1038/s43017-022-00296-7>.

© Springer Nature Limited 2022